Host cell perforation by listeriolysin O (LLO) activates a Ca^{2+}-dependent cPKC/Rac1/Arp2/3 signaling pathway that promotes *Listeria monocytogenes* internalization independently of membrane resealing

Jonathan G. T. Lam[a,b], Stephen Vadia[b], Sarika Pathak-Sharma[a], Eric McLaughlin[c], Xiaoli Zhang[c], Joel Swanson[d], and Stephanie Seveau[a,b,*]

[a]Department of Microbial Infection and Immunity, Infectious Diseases Institute, The Ohio State University Wexner Medical Center, Columbus, OH 43210; [b]Department of Microbiology and [c]Center for Biostatistics, The Ohio State University, Columbus, OH 43210; [d]Department of Microbiology and Immunology, University of Michigan Medical School, Ann Arbor, MI 48109-5624

ABSTRACT **Host cell invasion is an indispensable step for a successful infection by intracellular pathogens. Recent studies identified pathogen-induced host cell plasma membrane perforation as a novel mechanism used by diverse pathogens (*Trypanosoma cruzi*, *Listeria monocytogenes*, and adenovirus) to promote their internalization into target cells. It was concluded that *T. cruzi* and adenovirus damage the host cell plasma membrane to hijack the endocytic-dependent membrane resealing machinery, thereby invading the host cell. We studied *L. monocytogenes* and its secreted pore-forming toxin listeriolysin O (LLO) to identify key signaling events activated upon plasma membrane perforation that lead to bacterial internalization. Using various approaches, including fluorescence resonance energy transfer imaging, we found that the influx of extracellular Ca^{2+} subsequent to LLO-mediated plasma membrane perforation is required for the activation of a conventional protein kinase C (cPKC). cPKC is positioned upstream of Rac1 and the Arp2/3 complex, which activation leads to F-actin–dependent bacterial internalization. Inhibition of this pathway did not prevent membrane resealing, revealing that perforation-dependent *L. monocytogenes* endocytosis is distinct from the resealing machinery. These studies identified the LLO-dependent endocytic pathway of *L. monocytogenes* and support a novel model for pathogen uptake promoted by plasma membrane injury that is independent of membrane resealing.**

Monitoring Editor
William Bement
University of Wisconsin

Received: Sep 25, 2017
Revised: Nov 14, 2017
Accepted: Nov 20, 2017

INTRODUCTION

Intracellular pathogens use a large repertoire of virulence factors to subvert host cell machineries, thereby ensuring their life cycle and propagation within the infected host. An initial and indispensable step is the internalization of the pathogen into host cells (Cossart and Sansonetti, 2004; Cossart and Helenius, 2014). The present study elucidated a signaling pathway underlying a

This article was published online ahead of print in MBoC in Press (http://www.molbiolcell.org/cgi/doi/10.1091/mbc.E17-09-0561) on November 29, 2017.

The authors declare no competing financial interests.

Author contributions: J. G. T. L. designed and performed the experimental work and prepared figures, tables, and the article. S. V. and S. P.-S. performed experimental work and reviewed the article. E. M. and X. Z. performed statistical analyses. J. A. S. designed the experimental methods, provided constructs, and reviewed the article. S. M. S. designed the experiments and prepared the article.

*Address correspondence to: Stephanie Seveau (seveau.1@osu.edu).

Abbreviations used: ASM, acid sphingomyelinase; CDC, cholesterol-dependent cytolysin; cPKC, conventional protein kinase C; FRET, fluorescence resonance energy transfer; LLO, listeriolysin O; LLOpL, listeriolysin O prepore lock; mCFP, monomeric cyan fluorescent protein; mCit, monomeric Citrine; MyrPalm-CKAR, myristoylated and palmitoylated c kinase activity reporter; NC, negative control; PBD, p21-binding domain of PAK1; PI, propidium iodide.

unique mechanism of pathogen uptake by host cells, in which pathogens damage the host cell plasma membrane to promote their internalization.

The process of pathogen internalization into host cells can be passive from the perspective of the pathogen when a professional phagocyte uses its phagocytic receptors to engulf the pathogen (Brumell and Grinstein, 2003; Groves *et al.*, 2008; Stow and Condon, 2016). Alternatively, the uptake process can be active when pathogens express virulence factors that hijack the host cell endocytic pathways (Cossart and Sansonetti, 2004; Ham *et al.*, 2011; Ribet and Cossart, 2015; Pizarro-Cerda *et al.*, 2016). Although there is a high diversity of pathogens, they evolved common strategies to actively promote their internalization into host cells. Some pathogens use surface invasins that specifically activate a host receptor-mediated endocytic pathway (Isberg, 1990; Seveau *et al.*, 2007; Mercer and Helenius, 2012; Ribet and Cossart, 2015). Other pathogens use a secretion apparatus that injects effectors into the host cell cytosol. These effectors directly subvert signaling pathways that orchestrate the endocytic uptake of the pathogen (Brumell and Grinstein, 2003; Galan, 2009; Velge *et al.*, 2012; Mellouk and Enninga, 2016). Recent studies propose an additional invasion strategy that involves host cell plasma membrane perforation. Indeed, unrelated pathogens such as the eukaryotic parasite *Trypanosoma cruzi*, the bacterial pathogen *Listeria monocytogenes*, and the adenovirus HAdV-C2 perforate the host cell plasma membrane to promote their internalization into nonphagocytic cells (Fernandes *et al.*, 2011; Vadia *et al.*, 2011; Vadia and Seveau, 2014; Luisoni *et al.*, 2015). Some pathogens express several invasion factors and use multiple mechanisms to promote their internalization. Collectively, cooperation between these factors may increase the efficiency of host cell invasion. For example, to enter host cells *Salmonella* uses the surface invasin Rck and injects effectors via a type III secretion machinery (T3SS) (Rosselin *et al.*, 2010; Velge *et al.*, 2012; Wiedemann *et al.*, 2016). Adenoviruses can be internalized into host cells as a result of host receptor-mediated endocytosis and/or of plasma membrane injury (Bergelson *et al.*, 1997; Loustalot *et al.*, 2015; Luisoni *et al.*, 2015).

A particularity of the Gram-positive foodborne pathogen *L. monocytogenes* is its ability to infect a large diversity of cells including cells that are normally nonphagocytic such as enterocytes, hepatocytes, cytotrophoblasts, and neurons (Vazquez-Boland *et al.*, 2001). Therefore, it is not surprising that this pathogen uses multiple invasins and invasion strategies. *L. monocytogenes* expresses the surface invasins InlA and InlB to promote its internalization into cells that express the internalins receptors, E-cadherin and c-Met, respectively (Seveau *et al.*, 2004, 2007). Additionally, the secreted pore-forming toxin listeriolysin O (LLO) perforates the host cell plasma membrane to promote *L. monocytogenes* internalization into epithelial cells (Vadia *et al.*, 2011; Vadia and Seveau, 2014). LLO is a member of the MACPF/CDC (membrane attack complex perforin/cholesterol-dependent cytolysins) superfamily, which includes numerous eukaryotic pore-forming proteins and the largest family of bacterial pore-forming toxins, the CDCs (Rosado *et al.*, 2008; Seveau, 2014). CDCs form large β-barrel pores across cholesterol-containing membranes and are major virulence factors produced by Gram-positive pathogens. The CDC LLO and intermedilysin O (ILO), which is secreted by *Streptococcus intermedius*, induce bacterial internalization into human hepatocytes (Sukeno *et al.*, 2005; Vadia *et al.*, 2011).

Although numerous pathways for host receptor- and T3SS effector-mediated pathogen internalization have been extensively studied, less is known about the molecular machineries that link plasma membrane perforation to pathogen internalization. Recent studies have proposed that the pathway involved in resealing the damaged plasma membrane is directly responsible for pathogen uptake (Fernandes *et al.*, 2011; Andrews *et al.*, 2014; Luisoni *et al.*, 2015). Animal cells are frequently wounded due to numerous physical and biological stressors. For example, cells that compose contractile tissues, including those present in skeletal muscles or the intestinal tissue, are subject to mechanical stress. Cells throughout the body may also be exposed to pore-forming toxins produced by pathogens or by membrane-damaging agents released by the immune system. Owing to the frequency of these traumatic events and the inherent fragility of lipid bilayers, animal cells are able to rapidly reseal their plasma membrane to avoid necrosis or programmed cell death pathways. Several resealing mechanisms have been proposed including endocytosis of the damaged membrane (Tam *et al.*, 2010; Jimenez and Perez, 2017). It was proposed that the endocytic machinery that promotes membrane resealing is hijacked by pathogens such as *T. cruzi* and adenovirus to gain entry into host cells (Fernandes *et al.*, 2011; Luisoni *et al.*, 2015).

The present studies were designed to 1) identify key signaling events activated downstream from LLO-induced host cell plasma membrane perforation that mediate *L. monocytogenes* internalization and 2) delineate the potential involvement of membrane resealing in this signaling pathway. Together, our studies identified a novel endocytic pathway of *L. monocytogenes* and support a model for damage-dependent pathogen uptake that is independent of membrane resealing.

RESULTS

Rac1 is required for LLO-mediated internalization of *L. monocytogenes*

We previously showed that LLO pore formation was sufficient to induce F-actin–dependent *L. monocytogenes* internalization into epithelial cells (Vadia *et al.*, 2011). Because the Rho GTPases Rac1, Cdc42, and RhoA are master regulators of F-actin remodeling during bacterial internalization, we first established whether they were involved in the LLO-mediated entry pathway (Cox *et al.*, 1997; Etienne-Manneville and Hall, 2002; Sit and Manser, 2011). Expression of Rac1, RhoA, and Cdc42 was knocked down in human hepatocytes (HepG2) via treatment with silencing RNAs (siRNAs) for 48 h. The resulting knockdown efficiencies were assessed in each experiment by Western blot analysis of Rac1, RhoA, or Cdc42 in nontreated and siRNA-treated cells (Figure 1A). For each experiment, Rac1 protein level was decreased by 50–85% relative to negative control cells (NC) treated with NC siRNA, and RhoA and Cdc42 protein levels were decreased by more than 87% relative to NC cells (Figure 1A). Additionally, because these Rho GTPases can have overlapping activities, such as Rac1 and Cdc42 in the formation of lamellipodia (Hall, 2005), we also verified that silencing of one Rho GTPase did not result in a compensatory overexpression of the other two (Figure 1B). Densitometry analysis of the Western blots indicated that cell treatment with Rho GTPase-specific siRNAs does not result in compensatory expression of the two other Rho GTPases when compared with cells treated with NC siRNA (Supplemental Table S1). To determine the importance of these Rho GTPases for LLO-dependent internalization, nontreated and siRNA-treated cells were incubated with wild-type *L. monocytogenes* (WT, 10403s) or its isogenic LLO-deficient mutant (Δ*hly*) for 30 min at 37°C, and bacterial internalization (entry) efficiency was measured by immunofluorescence microscopy (Haghighat

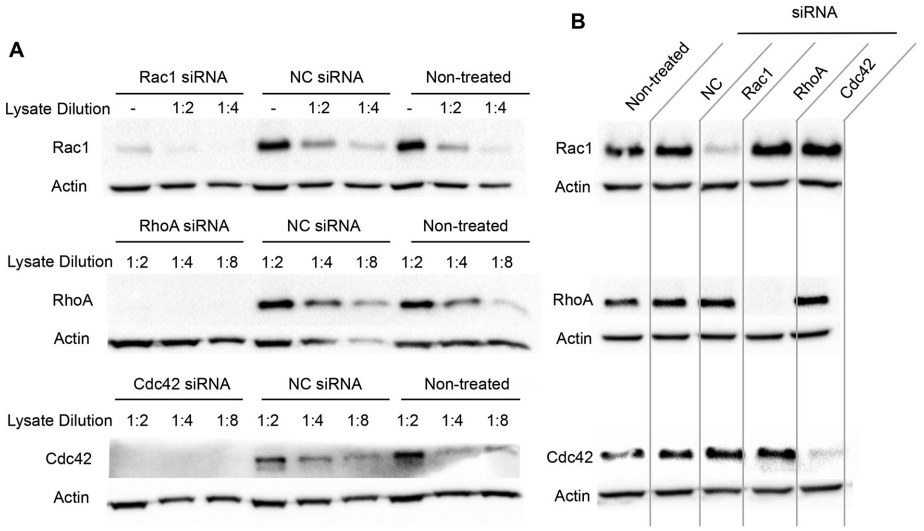

FIGURE 1: Rac1, RhoA, and Cdc42 knockdown efficiencies. (A, B) Western blot analysis of Rac1, RhoA, and Cdc42 in nontreated HepG2 cells and in HepG2 cells treated with a negative control siRNA (NC) or with Rac1-, RhoA-, or Cdc42-specific siRNAs. (A) Western blot analysis of cell lysates (nondiluted, 1:2, 1:4, and 1:8 diluted) using anti-Rac1, -RhoA, -Cdc42, and -actin antibodies. (B) Western blot analysis of nondiluted cell lysates to verify the absence of compensatory expression of Rac1 (top), RhoA (middle), or Cdc42 (bottom) in cells treated with Rac1-, RhoA-, and Cdc42-siRNAs. All Western blots are representative of at least three independent experiments.

and Seveau, 2010). In all treatment conditions, entry efficiencies of the LLO-deficient bacteria were less than 14% relative to entry of WT bacteria in NC siRNA-treated cells, further verifying that *L. monocytogenes* internalization is LLO dependent in HepG2 cells (Vadia *et al.*, 2011). Also, there was no significant difference in bacterial entry between the nontreated and NC siRNA-treated cells, showing that cell transfection did not alter bacterial uptake (Figure 2A). Knocking down Rac1 reduced entry of WT bacteria by 51.3 ± 3.2% ($p < 0.01$), whereas knocking down RhoA or Cdc42 did not significantly affect entry (Figure 2A). To further demonstrate the role of Rac1 in the LLO-mediated entry pathway in the absence of any other virulence factors, we measured the entry of 1-μm polystyrene beads coated with purified recombinant LLO. Beads were covalently coated with bovine serum albumin (BSA) followed by a noncovalent adsorption of LLO to mimic the release of LLO by bacteria (Vadia *et al.*, 2011). BSA-coated beads were used as a negative control. Nontreated and cells treated with NC-, Rac1-, RhoA-, and Cdc42-siRNAs were incubated with BSA- or BSA/LLO-coated beads for 30 min at 37°C and bead entry efficiency was measured by immunofluorescence microscopy. Relative to the NC siRNA treatment, Rac1-siRNA-treated cells exhibited a 61.8 ± 0.1% decrease in LLO-coated bead entry ($p < 0.005$). There was no statistically significant difference between RhoA and Cdc42 knockdown conditions relative to the NC siRNA-treated cells (Figure 2B).

On guanosine nucleotide exchange, the Rho GTPases undergo a conformational change into an active GTP-bound state, which permits their reversible association with downstream effectors such as p21 activated kinases (PAK) (Van Aelst and D'Souza-Schorey, 1997). We assessed whether Rac1 activation was required for the LLO-mediated entry pathway by utilizing a Rac1 dominant negative variant (Rac1N17) that is unable to bind GTP. HepG2 cells were transfected to express the fluorescent chimeras (monomeric Citrine) of native Rac1 (mCit-Rac1) or the dominant negative Rac1 variant (mCit-Rac1N17) (Hoppe and Swanson, 2004). Entry of BSA/LLO-coated beads into transfected, fluorescent cells expressing mCit-Rac1N17 was 74.6 ± 0.1% lower than cells expressing the native form of Rac1 ($p < 0.05$) (Figure 2C). Collectively, these data show that Rac1, but not RhoA or Cdc42, plays a crucial role in the LLO-mediated entry pathway of *L. monocytogenes*.

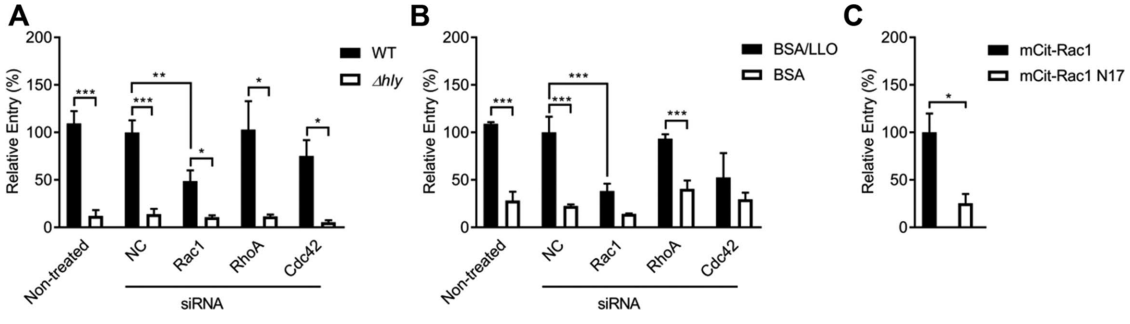

FIGURE 2: Role of Rac1 in LLO-dependent entry of *L. monocytogenes*. (A, B) Nontreated HepG2 cells and HepG2 cells treated with negative control (NC), Rac1-, RhoA-, and Cdc42-siRNAs were incubated with WT (10403s) or the LLO deficient (Δ*hly*) *L. monocytogenes* (A), or with BSA or BSA/LLO-coated beads (B), at a multiplicity of infection 20 (MOI 20) for 30 min at 37°C. (C) HepG2 cells expressing mCit-Rac1 or dominant negative mCit-Rac1N17 were incubated with BSA/LLO-coated beads at MOI 5 for 30 min at 37°C. Cells were then fixed and bacteria or beads were fluorescently labeled to enumerate the total number of bacteria (Nt) and the number of extracellular bacteria associated with host cells (Ne) (A, B, C). Entry efficiency was measured as 100 × [(Nt)-(Ne)]/(Nt) and results are expressed as the percentage entry ± SEM relative to NC-siRNA-treated cells incubated with WT (A) or BSA/LLO-coated polystyrene beads (B) ($n \geq 3$). In C, results are expressed as the percentage entry ± SEM relative to mCit-Rac1 expressing cells incubated with BSA/LLO-coated beads ($n = 4$). Statistics are as follows: *$p < 0.05$; **$p < 0.01$; ***$p < 0.005$.

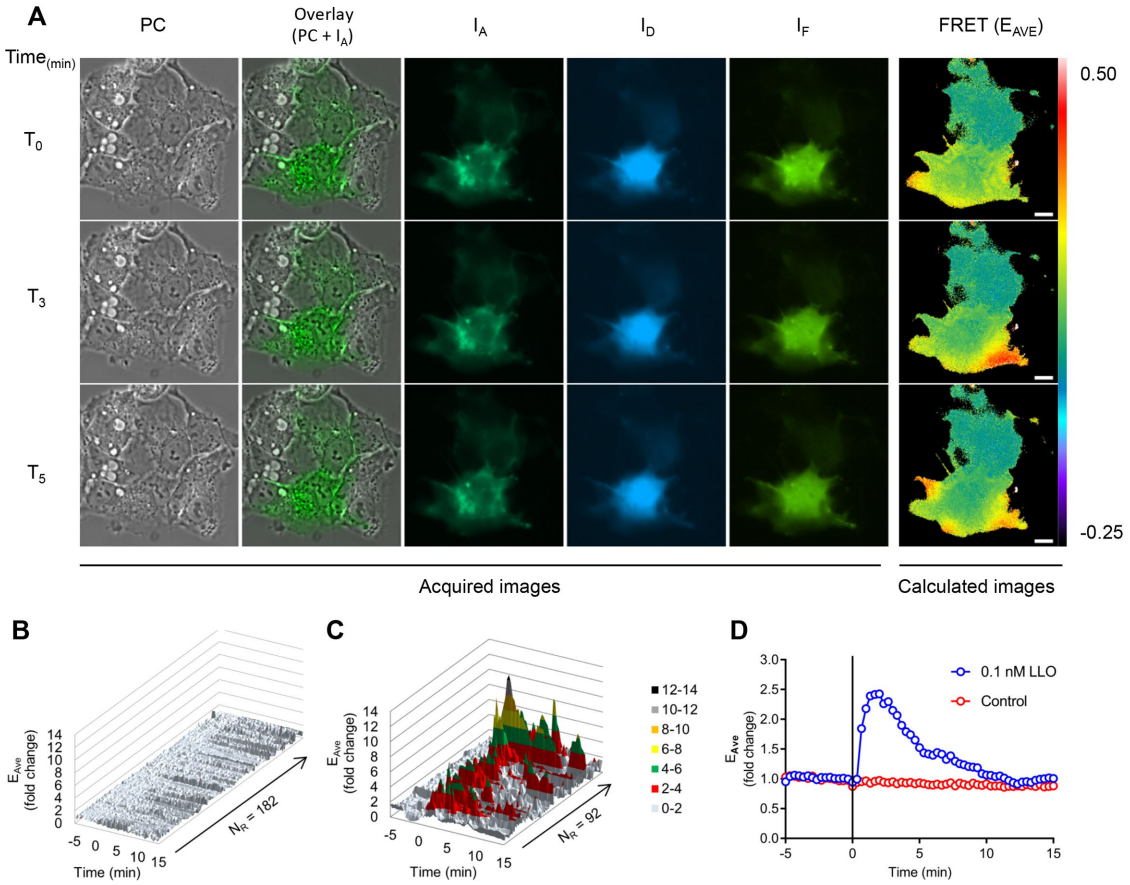

FIGURE 3: FRET stoichiometry to monitor Rac1 activation by LLO. HepG2 cells coexpressing mCFP-PBD and mCit-Rac1 were imaged on the microscope stage at 37°C. Phase-contrast (PC), and fluorescence images (I_A, I_D, and I_F) were acquired every 20 s for 20 min. LLO was added after 5 min of imaging (T_0). (A) PC, overlay of PC and I_A, I_A, I_D, I_F, and FRET (E_{AVE} presented in pseudocolor scale). Scale bar = 10 µm. From top to bottom: time points 0, 3, and 5 min after addition of LLO. (B, C) For each imaged cell, two regions of standard size (305 pixels) were applied at locations where FRET variations were observed. If no FRET variation was observed, then the regions were arbitrarily positioned. The *y*-axis indicates the fold change in E_{AVE} and the *z*-axis represents all individual regions of control cells (182 regions, 91 cells) (B), and all FRET-positive regions from the LLO-exposed cells (92 regions, 57 cells) (C), in which FRET positive is defined as a greater than twofold increase in FRET efficiency ($n = 3$). (D) Kinetics of the averaged E_{AVE} of control (182) and LLO-exposed (92) regions. The black vertical line indicates the time of addition of medium alone (control) or 0.1 nM LLO.

Rac1 activation by LLO is pore and Ca^{2+} influx dependent

To confirm that LLO is sufficient to activate Rac1, we monitored the spatiotemporal dynamics of Rac1 activation in living cells using a fluorescence resonance energy transfer– (FRET) based fluorescence microscopy method (Hoppe *et al.*, 2002; Hoppe and Swanson, 2004). HepG2 cells cotransfected to express the FRET-pair mCit-Rac1 and monomeric cyan fluorescent protein–p21-binding domain (mCFP-PBD) were imaged in an atmosphere-controlled, wide-field fluorescence microscope. In this system, Rac1 activation leads to the formation of the complex mCit-Rac1/mCFP-PBD, resulting in the generation of a FRET signal that can be analyzed quantitatively using the FRET stoichiometry method (Hoppe *et al.*, 2002; Hoppe and Swanson, 2004) (Supplemental Figure S1 and Supplemental Movie S1). Cells that coexpressed mCFP-PBD and mCit-Rac1 were imaged for 5 min before the addition of physiologically relevant concentrations of LLO (0.1 nM). Importantly, this toxin concentration is nonlethal and sufficient to induce the entry of LLO-deficient *L. monocytogenes* and BSA-coated beads when LLO is added exogenously to the cell culture medium (Vadia, Arnett *et al.*, 2011). LLO-exposed cells exhibited elevated levels of Rac1 activation, as evidenced by transient FRET flashes that paralleled the appearance and disappearance of membrane ruffles in successive waves at different cellular locations (Figure 3A and Supplemental Movie 1). Because Rac1 was activated only within discrete cell regions in a transient manner, we quantified Rac1 FRET in regions of standard size that were positioned where Rac1 activation was observed or positioned arbitrarily if Rac1 activation was absent. Two regions of standard size were positioned on each cell and were analyzed whether Rac1 FRET fluctuations were observed. Data show that Rac1 activation was detected in 76.61% of cells exposed to LLO (Table 1; corresponding statistical analyses in Supplemental Table S2). Rac1 activation was defined as an at least twofold increase in FRET efficiency within the analyzed region (FRET-positive region). In contrast, only 2.43% of control cells (not exposed to LLO) were positive for Rac1 FRET. Rac1 activation kinetics measured in all regions and kinetics of Rac1 activation averaged across all regions are presented in Figure 3, B–D. This analysis showed that at the cell population level, Rac1 was activated ~40 s after addition of LLO with a maximal amplitude at 80–120 s for a duration of 2 min. Statistical analyses of the FRET kinetics presented in Figure 3 are presented in Supplemental Table S3. To

Toxin	–	LLO	LLOpL (0.1 nM)	LLOpL (10 nM)	–	LLO	–	LLO
Medium ($CaCl_2$)	+	+	+	+	+	+	–	–
Time (min)	20	20	20	20	10	10	10	10
N_C	91	75	164	148	91	75	125	173
$FRET^+$ cells	3	57	9	12	0	56	8	10
% FRET	2.43	76.61	5.88	7.22	0	74.83	4.78	5.68

Cells were exposed, or not, to 0.1 nM LLO, 0.1 nM LLOpL, and 10 nM LLOpL in cell culture medium with (+) or without (–) $CaCl_2$. Time indicates the total duration of imaging. In Ca^{2+}-free medium (–) cells were imaged for only 10 min due to cell damages caused by LLO. N_C is the number of analyzed cells. $FRET^+$ cells is the number of FRET-positive cells (exhibiting at least twofold increase in FRET). % FRET is the percentage of FRET-positive cells ($n > 3$).

TABLE 1: LLO induces Rac1 activation in a Ca^{2+}- and pore-dependent manner.

establish the role of LLO pore formation in Rac1 activation, cells were exposed to an LLO variant (listeriolysin O prepore lock, LLOpL) that binds to the host cell plasma membrane and forms a prepore complex but is unable to transition into the transmembrane β-barrel pore (Hotze *et al.*, 2001; Vadia *et al.*, 2011). Indeed, LLOpL was shown to be inactive at concentrations exceeding 10^4 nM as compared with native LLO (EC_{50} = 1 nM), but its pore-forming activity was restored to the native LLO level upon treatment with 4 mM dithiothreitol (DTT) (Supplemental Figure S2A) (Seveau, 2014). Treatment with 0.1 and 10 nM LLOpL failed to activate Rac1 in HepG2 cells (Table 1; statistical analyses in Supplemental Table S2). Thus, as reported for LLO-dependent *L. monocytogenes* entry and membrane ruffling, Rac1 activation requires LLO pore formation (Vadia *et al.*, 2011). Formation of the transmembrane pore leads to an influx of extracellular Ca^{2+}, which is required for LLO-mediated *L. monocytogenes* entry (Vadia and Seveau, 2014). To prevent Ca^{2+} influx, cells were analyzed in Ca^{2+}-free medium. Because the influx of Ca^{2+} is indispensable for membrane resealing, for in the absence of extracellular Ca^{2+} cell integrity is rapidly compromised upon damage, FRET analysis was limited to time points 0–5 min post–LLO exposure (Vadia and Seveau, 2014). In the absence of extracellular Ca^{2+}, LLO-induced Rac1 activation occurred in 5.68% of cells compared with 74.83% in the presence of extracellular Ca^{2+} (Table 1; statistical analyses in Supplemental Table S2). Collectively, these data establish that LLO is sufficient to activate Rac1 within membrane ruffles in a pore- and Ca^{2+}-influx–dependent manner.

LLO-mediated Rac1 activation results in Arp2/3-dependent F-actin remodeling

The subcortical F-actin cytoskeleton acts as a dynamic scaffold that promotes the formation of membrane ruffles and the formation of the phagocytic cup (Rougerie *et al.*, 2013). We used a live-cell fluorescence imaging approach to visualize F-actin rearrangement in Tomato-β-actin-expressing HepG2 cells. We could clearly visualize the formation of F-actin bundles within membrane ruffles in cell exposed to LLO (Figure 4 and Supplemental Movie 2). We observed by live-cell phase-contrast imaging that 85% of cells exposed to LLO initiated membrane ruffling as early as 84.8 ± 26.7 s (average ± SD; >100 cells, n = 8) following exposure to LLO. Additionally, LLO-induced membrane ruffling was frequently followed by the formation of large endocytic vacuoles reminiscent of macropinosomes (Supplemental Movie 3). F-actin polymerization can involve two types of actin nucleators: formins and the Arp2/3 complex (Chesarone and Goode, 2009). Because Arp2/3 is most commonly involved in remodeling F-actin at bacterial entry sites, we focused on establishing the role of the Arp2/3 complex in HepG2 cells exposed to LLO in the presence or absence of the Arp2/3 inhibitor CK-666 (Hetrick *et al.*, 2013). Inhibition of Arp2/3 abolished LLO-induced membrane ruffling, as assessed by live cell phase-contrast imaging (0% of cells exhibited membrane ruffling; >100 cells, n = 3) as compared with control cells (85%, >100 cells, n = 3; Supplemental Movies 4 and 5). Therefore, LLO induces Arp2/3-dependent de novo F-actin remodeling and subsequent membrane ruffling. To establish whether Rac1 activation occurs upstream from Arp2/3-dependent F-actin remodeling, cells were transfected to express fluorescent chimeras of the native (mCit-Rac1)- or dominant-negative (mCit-Rac1N17)-Rac1 or fluorophore alone (mCit). In cells expressing the fluorophore alone (126 cells, n = 3) or mCit-Rac1 (112 cells, n = 3) 75.4% and 58.04% of cells exhibited membrane ruffling in response to LLO, respectively. However, cells expressing mCit-Rac1N17 (114 cells, n = 3) exhibited substantial decrease in membrane ruffling upon LLO exposure (6.14% ruffling). As expected, nonfluorescent

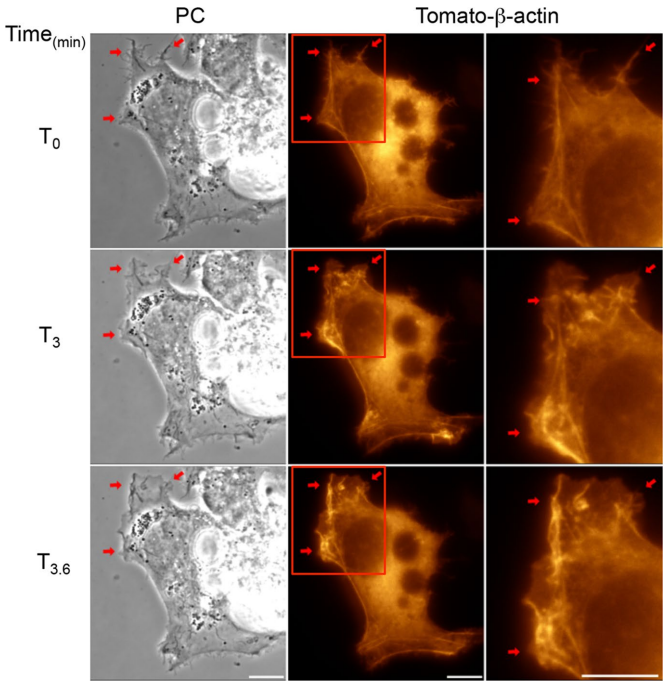

FIGURE 4: LLO induces F-actin rearrangement. HepG2 cells expressing Tomato-β-actin were imaged on the microscope stage at 37°C. Phase-contrast (PC, column 1), and fluorescence images were acquired every 20 s for 20 min. LLO was added after 5 min of imaging (T_0). LLO induces dynamic F-actin rearrangement (red arrows) within membrane ruffles. Regions highlighted in column 2 are shown in column 3. Scale bar = 10 μm.

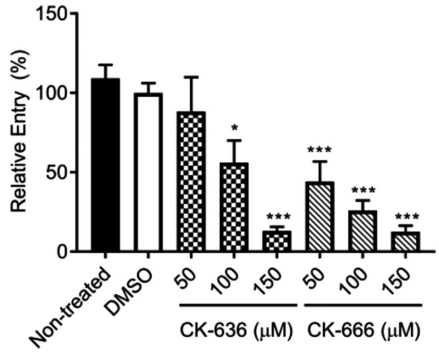

FIGURE 5: Role of Arp2/3 in LLO-dependent entry of *L. monocytogenes*. Nontreated and cells treated with 0.2% DMSO or the Arp2/3 inhibitors CK-636 and CK-666 were infected with WT *L. monocytogenes* at MOI 20 for 30 min at 37°C. Cells were fixed, and bacteria were fluorescently labeled to enumerate the total number of bacteria (Nt) and the number of extracellular bacteria associated with host cells (Ne). Entry efficiency was measured as 100 × [(Nt) − (Ne)]/(Nt), and results are expressed as the mean percentage entry ± SEM relative to the DMSO control. Statistics are as follows: *$p < 0.05$; ***$p < 0.005$ ($n = 3$).

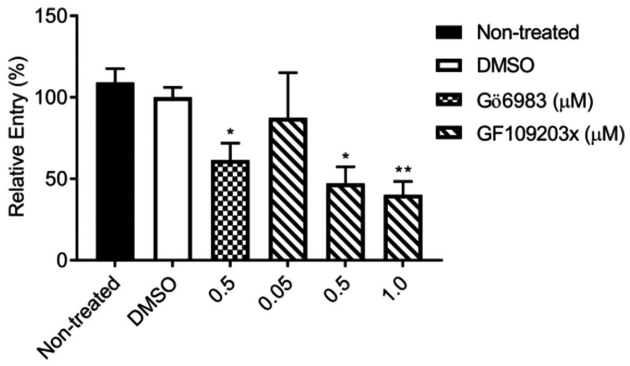

FIGURE 6: Role of a conventional PKC in LLO-dependent entry of *L. monocytogenes*. Nontreated and cells treated with 0.2% DMSO, the broad spectrum (Gö6983) or conventional (GF109203x) PKC inhibitors, were infected with WT *L. monocytogenes* at MOI 20 for 30 min at 37°C. Cells were chemically fixed, and bacteria were fluorescently labeled to enumerate the total number of bacteria (Nt) and the number of extracellular bacteria associated with host cells (Ne). Entry efficiency was measured as 100 × [(Nt) − (Ne)]/(Nt), and results are expressed as the mean percentage entry ± SEM relative to the DMSO control. Statistics are as follows: *$p < 0.05$; **$p < 0.01$ ($n = 3$).

neighboring cells that did not express mCit-Rac1N17 exhibited membrane ruffling, further supporting the hypothesis that Rac1 activation is a prerequisite for LLO-induced membrane ruffling (Supplemental Movie 6). Importantly, we also established that the Arp2/3 complex is required for *L. monocytogenes* entry into HepG2 cells using the Arp2/3 inhibitors CK-636 and CK-666. Figure 5 shows the dose-dependent inhibition of *L. monocytogenes* entry by the Arp2/3 inhibitors, indicating that the same machinery that is driving LLO-mediated F-actin–dependent remodeling is also necessary for *L. monocytogenes* internalization. Collectively, our data indicate that LLO-mediated entry involves Rac1 activation upstream from Arp2/3-dependent F-actin remodeling.

A conventional PKC is required for LLO-mediated entry of *L. monocytogenes*

The conventional Ca^{2+}-responsive PKC alpha (PKCα) has been shown to be involved in Rac1 translocation to the plasma membrane of cells treated with thapsigargin or ionomycin, which, similarly to LLO, cause an increase in cytosolic Ca^{2+} (Price *et al.*, 2003). To determine whether a PKC is involved in *L. monocytogenes* internalization into HepG2 cells, we measured *L. monocytogenes* entry into cells pretreated with broad spectrum (Gö6983) and conventional (GF109203x) PKC inhibitors. Treatment with 0.5 μM Gö6983 or 1 μM GF109203x resulted in a 59.9 ± 1.5% ($p < 0.05$) and 61.5 ± 1.9% ($p < 0.01$) decrease in *L. monocytogenes* entry, respectively, relative to the vehicle control, indicating a role for a conventional PKC (Figure 6).

A conventional PKC is activated by the influx of extracellular Ca^{2+} leading to Rac1 activation

We then focused on demonstrating the activation of a PKC by LLO. We transfected HepG2 cells with fluorescent chimeras of two conventional (α, βII) and two novel (ε, δ) PKC isoforms. HepG2 cells exposed to LLO exhibited dynamic translocation of GFP-PKCα (translocation was observed in 70.8% of transfected cells; 250 cells, $n = 7$; Figure 7 and Supplemental Movie 7), GFP-PKCε (63.63%; 22 cells, $n = 1$), and GFP-PKCβII (37.5%; 24 cells, $n = 1$), but not of GFP-PKCδ (0%; 65 cells, $n = 2$) or GFP alone (0%; 32 cells, $n = 1$; Supplemental Movie 7) to regions of plasma membrane ruffles as early as 40 s after addition of LLO. We further established that the influx of extracellular Ca^{2+} was indispensable for PKC translocation, as observed in cells exposed to LLO in Ca^{2+}-free medium (0% of GFP-PKCα translocation, 23 cells, $n = 1$; Supplemental Movie 8). Importantly, cells treated with the conventional PKC inhibitor GF109203x did not undergo F-actin–dependent membrane ruffling in response to LLO exposure (3.5% of cells exhibited membrane ruffling, >100 cells, $n = 3$), suggesting that a Ca^{2+}-responsive conventional PKC was involved in Rac1 activation. To demonstrate that LLO activates a PKC, we used the PKC FRET biosensor myristoylated and palmitoylated c kinase activity reporter (MyrPalm-CKAR), which has a 20% dynamic range and was designed to specifically assess PKC activity at the plasma membrane (Violin *et al.*, 2003; Gallegos and Newton, 2011). In the nonphosphorylated state, MyrPalm-CKAR exists in a constrained conformation that places the N-terminal mCFP in close proximity to the C-terminal mCit leading to FRET, but phosphorylation of the interconnecting sequence by any PKC isoform relaxes the sensor leading to a loss of FRET. We tested whether addition of the Ca^{2+} ionophore, ionomycin, which is known to activate PKCs, would lead to pronounced phosphorylation of the biosensor. As expected, addition of ionomycin resulted in a sudden drop in FRET efficiency followed by a quick recovery (Supplemental Figure S3). This result is consistent with the notion that Ca^{2+} influx leads to activation of PKC at the plasma membrane followed by dephosphorylation of the biosensor thereafter, as previously observed in mouse oocytes (Gonzalez-Garcia *et al.*, 2013). HepG2 cells expressing MyrPalm-CKAR and exposed to LLO exhibited an initial drop in FRET, that is, MyrPalm-CKAR phosphorylation, 40 s after addition of LLO, which overlays with the kinetics of PKCα translocation and Rac1 activation (Figure 8, Supplemental Movie 9, and statistical analyses in Supplemental Table S4). The magnitude of change in FRET efficiency in LLO-exposed cells is 65% lower than observed in ionomycin-treated cells, but the duration of PKC activity is prolonged, which may be due to smaller and prolonged Ca^{2+} fluxes in LLO-exposed cells. Importantly, LLO-induced MyrPalm-CKAR phosphorylation was inhibited by cell pretreatment with the conventional

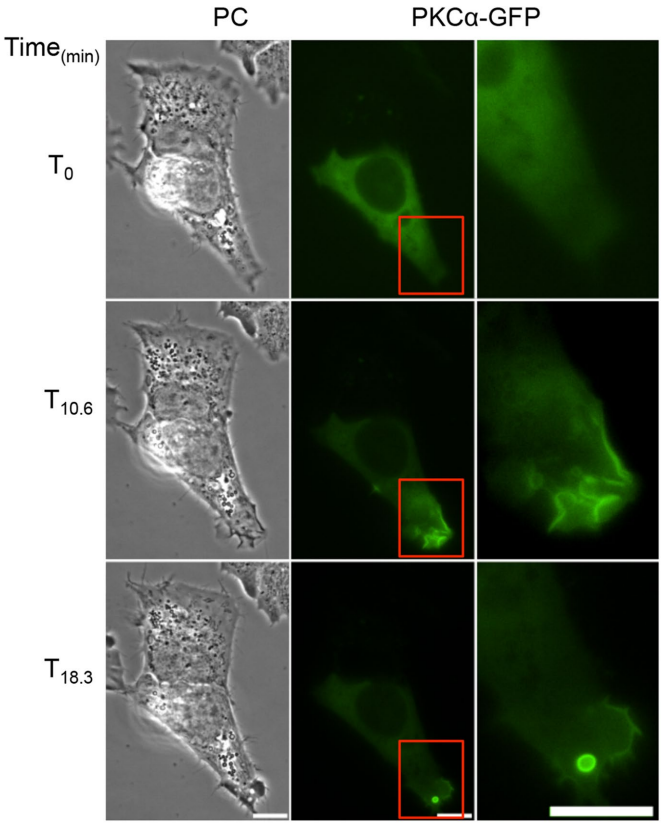

FIGURE 7: LLO induces PKCα translocation to the plasma membrane. HepG2 cells expressing GFP-PKCα were imaged on the microscope stage at 37°C. Phase-contrast (PC), and fluorescence images were acquired every 20 s for 20 min. LLO was added after 5 min of imaging (T_0). LLO induces GFP-PKCα translocation to regions of dynamic plasma membrane ruffles and around newly formed vesicles. Regions highlighted in column 2 are shown in column 3. Scale bar = 10 μm.

PKC inhibitor GF109203x (Figure 8). We then established whether a conventional PKC was involved in Rac1 activation. Rac1 activation was measured by FRET stoichiometry as presented in Figure 3. We found that Rac1 was no longer activated by LLO in cells pretreated with the conventional PKC inhibitor GF109203x (Table 2; statistical analyses in Supplemental Table S5). Collectively, our data show that a conventional PKC links Ca^{2+} influx to Rac1 activation and Arp2/3-dependent F-actin remodeling for bacterial internalization.

Inhibition of the LLO-mediated entry pathway facilitates membrane resealing

We previously showed that cells exposed to physiological concentrations of LLO undergo rapid Ca^{2+}-dependent membrane resealing (Vadia and Seveau, 2014). To investigate if LLO-mediated *L. monocytogenes* entry pathway is part of the membrane resealing machinery, we measured the efficiency of membrane resealing in cells pretreated with the inhibitors that prevent LLO-induced *L. monocytogenes* entry (Pathak-Sharma *et al.*, 2017). HepG2 cells were incubated with inhibitors of conventional PKC, Arp2/3, or F-actin and exposed to LLO. As a control, inhibition of membrane resealing was achieved by incubating cells in Ca^{2+}-free medium. These experiments were performed in the presence of the plasma membrane-impermeant nucleic acid–binding probe propidium iodide. Propidium iodide flows through damaged cell membranes, leading to a strong, quantifiable fluorescence signal, whereas cells with intact plasma membranes exclude the probe or are minimally labeled. We found that HepG2 cells treated with the conventional PKC inhibitor, the Arp2/3 inhibitor, or the F-actin inhibitor and exposed to LLO, resealed their plasma membrane more efficiently than cells treated with LLO (+ vehicle) in the absence of inhibitors (Figure 9). Indeed, statistical analyses revealed that the presence of the inhibitors improved cell integrity ($p < 0.0001$). Importantly, LLO pore-forming activity was not altered by any of these inhibitors (Supplemental Figure S2b). In conclusion, LLO pore formation was followed by F-actin–independent membrane resealing and by F-actin–dependent bacterial entry. Both processes were initiated by the influx of extracellular Ca^{2+}, but involved distinct signaling pathways thereafter.

DISCUSSION

This study identified a signaling pathway activated by the pore-forming toxin listeriolysin O (LLO) to promote the internalization of the bacterial pathogen *L. monocytogenes* into human hepatocytes. LLO is an exotoxin that forms large pores across the host cell plasma membrane causing a rapid influx of extracellular Ca^{2+}. Ca^{2+} influx is then involved in the translocation and activation of conventional protein kinase C (cPKC) at the plasma membrane. Subsequently, the cPKC is required for Rac1 activation upstream of Arp2/3-dependent de novo assembly of the F-actin cytoskeleton for *L. monocytogenes* internalization (Figure 10). This is the first identification of a signaling pathway activated downstream from plasma membrane perforation by a pore-forming toxin leading to the internalization of a bacterial pathogen. Because pore-forming toxins are virulence factors produced by a large diversity of pathogens, perforation of the host cell plasma membrane is likely a ubiquitous mechanism by which pathogens hijack signaling to enter host cells. Importantly, this work also shows that the identified pathway is dispensable for efficient resealing of the plasma membrane. Although membrane resealing is required for *L. monocytogenes* internalization, for in its absence cell integrity is lost, the signaling pathway directing F-actin remodeling at the bacterial entry site is distinct from the membrane resealing pathway.

Link between pathogen internalization and resealing of the injured plasma membrane

Studies on the eukaryotic parasite *T. cruzi* and the adenovirus HadV-C2 proposed that pathogens damage the host cell plasma membrane and co-opt the subsequent membrane repair machinery to promote their endocytosis (Fernandes *et al.*, 2011; Luisoni *et al.*, 2015). It is thought that flagellar-mediated motility of *T. cruzi* induces mechanical damages and that the adenovirus perforates the cell by uncoating of the membrane damaging protein-VI. Both studies support the hypothesis that cell injury leads to the influx of extracellular Ca^{2+}, which promotes plasma membrane resealing via the following sequence of events: Ca^{2+}-dependent exocytosis of lysosomes, release of the lysosomal enzyme acid sphingomyelinase (ASM), conversion of sphingomyelin into ceramide by ASM on the outer leaflet of the plasma membrane, and ceramide-mediated endocytosis (Andrews *et al.*, 2014). This pathway leads to the endocytosis of the damaged membrane together with the pathogen (Tam *et al.*, 2010). Furthermore, it was established that resealing is independent of F-actin, dynamin, and clathrin, but requires caveolin-rich membrane microdomains (Corrotte *et al.*, 2013; Andrews *et al.*, 2014). While the evidence supports that membrane resealing is required for pathogen internalization, it is unclear whether the membrane resealing process is directly responsible or whether it is a prerequisite for pathogen uptake. In the latter hypothesis,

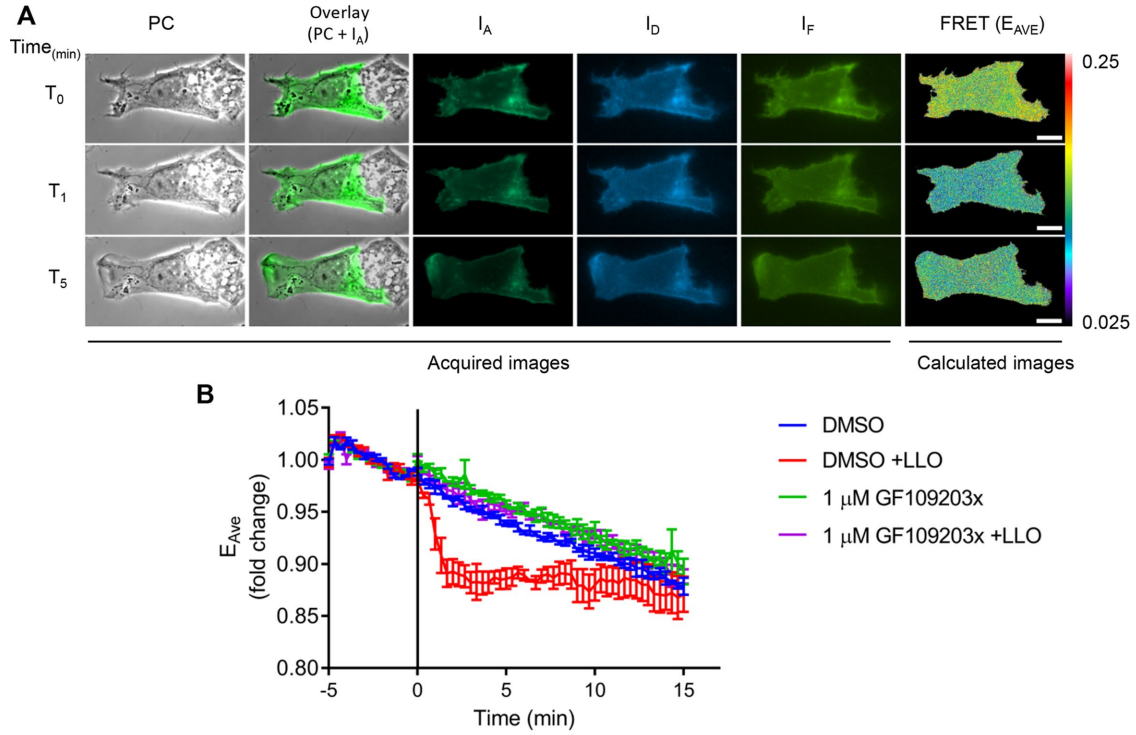

FIGURE 8: A PKC is activated by LLO. HepG2 cells expressing MyrPalm-CKAR were imaged on the microscope stage at 37°C. Phase-contrast (PC) and fluorescence images (I_A, I_D, and I_F) were acquired every 20 s for 20 min. LLO was added after 5 min of imaging (T_0 and black vertical line). (A) A representative cell exhibiting LLO-induced MyrPalm-CKAR phosphorylation. From left to right: PC, overlay of PC + IA, I_A, I_D, and I_F, and FRET (in pseudo-color scale). From top to bottom: time points 0, 1, and 5 min after addition of LLO. Scale bar = 10 μm. (B) Data are presented as the average fold change in E_{AVE} ± SEM (n = 3, 24 cells in DMSO control, 26 cells in GF109203x, 28 cells in DMSO +LLO, and 26 cells in GF109203x +LLO).

resealing would be necessary to maintain cell homeostasis and allow for a distinct pathway to promote uptake of the pathogen. Our studies favor the latter hypothesis. Indeed, we identified signaling events required for LLO-dependent *L. monocytogenes* internalization that were dispensable for membrane resealing. Inhibition of cPKC, Arp2/3, and F-actin assembly improved the efficiency of cell resealing (Figure 9) without altering LLO pore formation (Supplemental Figure S2b). Similar to previous studies, we found that resealing of cells damaged by LLO is independent of F-actin, clathrin, and dynamin (Vadia *et al.*, 2011). Therefore, the resealing machinery downstream from LLO perforation is expected to proceed via the same pathway as described for *T. cruzi* and adenovirus, but LLO-induced *L. monocytogenes* endocytosis does not directly involve the resealing machinery. In accordance with our findings, studies have also identified roles for cPKC and F-actin reorganization in entry of adenovirus and *T. cruzi* into nonprofessional phagocytes (Li *et al.*, 1998; Woolsey and Burleigh, 2004; Maeda *et al.*, 2012; Yousuf *et al.*, 2016). Whether or not *T. cruzi* and adenovirus utilize the resealing machinery or the signaling pathway described in this work to gain entry into cells, pathogen-mediated host plasma membrane damage represents an invasion mechanism broadly used by unrelated pathogens.

Role of F-actin remodeling in *L. monocytogenes* uptake and in membrane resealing

Internalization of most pathogens requires F-actin remodeling for the formation of the endosome that contains the pathogen. This was demonstrated for most, if not all, bacterial pathogens, including *L. monocytogenes* invasion of professional phagocytes and normally nonphagocytic cells as well as for the endocytosis of viruses, such as the adenovirus and for *T. cruzi* invasion of nonphagocytic cells (Li *et al.*, 1998; Wang *et al.*, 1998; Fernandes *et al.*, 2013). Similarly, the LLO-dependent *L. monocytogenes* entry pathway is dependent on de novo F-actin assembly (Vadia *et al.*, 2011). A point of convergence is that an intact F-actin cytoskeleton is not required for resealing the plasma membrane during pathogen uptake (Idone, Tam *et al.*, 2008; Fernandes *et al.*, 2011; Vadia and Seveau, 2014). Plasma membrane resealing is thought to require initial disassembly of cortical F-actin to 1) clear the way for docking and fusion of

Toxin	—	LLO	LLO
Medium	DMSO	DMSO	GF109203x
Time (min)	20	20	20
N_C	115	92	136
$FRET^+$ cells	1	50	26
% FRET	0.87	54.3	19.12

Cells were exposed to DMSO (0.2%), 0.1 nM LLO, or GF109203x. Time indicates the total duration of imaging. N_C is the number of analyzed cells. $FRET^+$ cells is the number of FRET-positive cells (exhibiting at least a twofold increase in FRET). % FRET is the percentage of FRET-positive cells (n > 3).

TABLE 2: Rac1 is activated downstream of a conventional PKC.

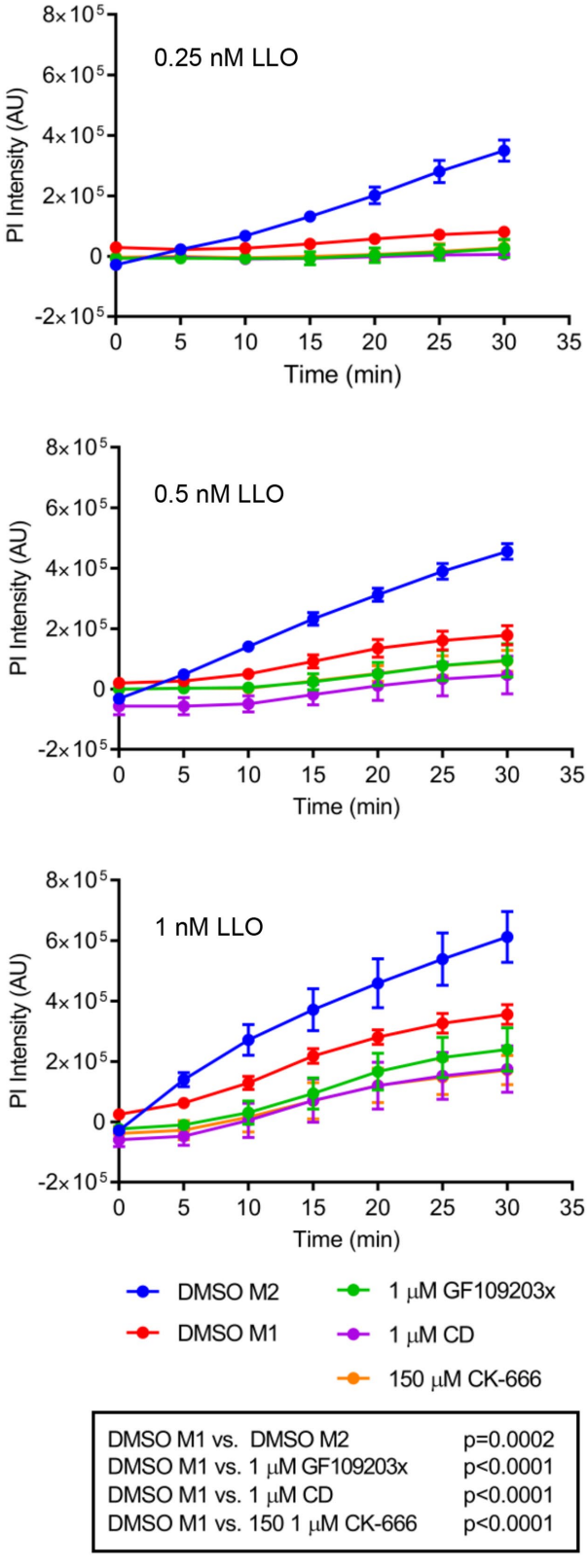

DMSO M1 vs. DMSO M2	p=0.0002
DMSO M1 vs. 1 μM GF109203x	p<0.0001
DMSO M1 vs. 1 μM CD	p<0.0001
DMSO M1 vs. 150 1 μM CK-666	p<0.0001

FIGURE 9: The LLO-dependent entry pathway is dispensable for membrane resealing. HepG2 cells were plated in a 96-well plate and incubated in the presence of DMSO (control), GF109203x, cytochalasin D (CD), or CK-666 in Ca^{2+}-containing medium (M1) or in DMSO in Ca^{2+}-free medium (M2, control for membrane repair). Cells were exposed to 0.25, 0.5, or 1 nM LLO, and the fluorescence intensity of propidium iodide (PI) was measured in the plate reader every 5 min for 30 min at 37°C. Experimental triplicates were performed for each condition, and three independent experiments were performed. Data are presented as the average PI intensity ± SEM. Statistical analyses were performed as described under *Materials and Methods* and are presented in the text box ($n = 3$).

lysosomes with the plasma membrane and 2) decrease surface tension, which prevents enlargement of the plasma membrane wound (Cooper and McNeil, 2015). In accordance with this model, our data show that inhibiting signaling events that favor F-actin assembly improves plasma membrane resealing (Figure 9). Thus, how does one explain that cells undergo de novo F-actin assembly in response to perforation by LLO if F-actin assembly is dispensable for resealing? Similarly to our observation, membrane damage in *Xenopus laevis* oocytes was followed by Rho GTPase activation and F-actin assembly (Simon *et al.*, 2013). In this example, F-actin assembly was proposed to facilitate repair of very large mechanical wounds. It is possible that injured cells respond to wounding by a sequence of events that include initial disassembly of the actin network followed by its reassembly, regardless of the nature of the wound. We propose that F-actin reassembly 1) repairs large mechanical wounds but is dispensable for repairing smaller injuries caused by toxin pores and 2) restores the cortical F-actin network. Alternatively, one can propose that the reassembly of the F-actin network is due to an additional property of LLO.

LLO is sufficient to activate cPKC-, Rac1-, and Arp2/3-dependent F-actin remodeling

LLO is a multifunctional toxin that affects transcriptional regulation, protein ubiquitination, and mitochondrial dynamics (Hamon *et al.*, 2006; Gonzalez *et al.*, 2011; Seveau, 2014; Osborne and Brumell, 2017). The present studies identified LLO as a regulator of the F-actin cytoskeleton. To monitor the spatiotemporal dynamics of signaling events downstream from LLO pore formation, we used a highly sensitive live-cell FRET-based approach that quantitatively detects small changes in protein activation in single cells (Hoppe *et al.*, 2002; Hoppe and Swanson, 2004). This approach revealed that the kinetics of PKC activation overlay and potentially precede Rac1 activation, a fact that we confirmed with pharmacological inhibitors (Figures 3 and 8). Interestingly, Rac1 activation proceeded in a wavelike pattern, reminiscent of calcium waves. This could be observed because we used a fluorescent chimera of native Rac1. However, the MyrPalm-CKAR biosensor is artificially anchored to the plasma membrane, which allows us to monitor the kinetics of PKC activation at this location, but not native PKC translocation (Violin *et al.*, 2003; Gallegos and Newton, 2011; Antal *et al.*, 2014). To assess PKC translocation, we used cells expressing fluorescent chimeras containing the membrane-binding domains of the PKC isoforms PKCα, PKCβII, and PKCε. Fluorescent cPKC domains were translocated to regions of the membrane where membrane ruffles and macropinosomes were formed similarly to the Rac1 activation pattern (Figure 7 and Supplemental Movie 7). The present work demonstrates for the first time the activation of a conventional PKC by LLO. Previous studies reported the activation of the calcium-independent PKCε (novel PKC) (Shaughnessy *et al.*, 2007). Because activation of conventional and novel PKC requires production of diacylglycerol (DAG), LLO may also activate host phospholipases, as previously suggested (Shaughnessy *et al.*, 2007). Our finding that Ca^{2+} influx leads to cPKC activation upstream to Rac1 is reminiscent of previous work using the calcium ionophore ionomycin (Price *et al.*, 2003). In that study, a cPKC

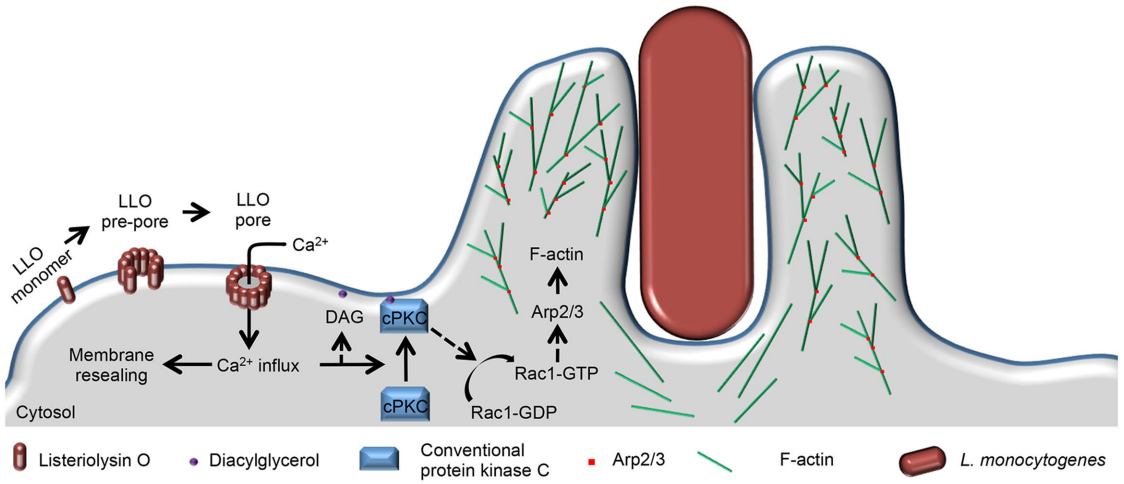

FIGURE 10: Model for LLO-mediated *L. monocytogenes* entry. *L. monocytogenes* secretes the pore-forming toxin listeriolysin O (LLO), which binds to the cholesterol-rich plasma membrane and oligomerizes into a prepore complex. The prepore complex then transitions into a transmembrane pore, which permits the influx of extracellular Ca^{2+}. A rise in cytosolic Ca^{2+} results in the translocation and activation of a conventional PKC at the plasma membrane. Activated PKC promotes the activation of the Rho GTPase Rac1, which transduces the signal down to induce Arp2/3-mediated F-actin remodeling at the plasma membrane leading to *L. monocytogenes* entry. The influx of extracellular Ca^{2+} also induces a membrane resealing pathway.

responsive to Ca^{2+} influx phosphorylated a RhoGDI facilitating Rac1 activation (Price *et al.*, 2003). Thus, the influx of Ca^{2+} through LLO pores could suffice to activate Rac1 in a similar manner. This idea is supported by the dependence of PKC and Rac1 activation on Ca^{2+} influx and the fact that the prepore-locked form of LLO (LLOpL) was inactive. In accordance with our results, the *Streptococcus pneumoniae* CDC pore-forming toxin pneumolysin induces Ca^{2+}-dependent F-actin remodeling in a Rho GTPase (Rac1, Cdc42, and RhoA)-dependent manner (Iliev *et al.*, 2007). Our FRET studies established that LLO also activates Cdc42 (Supplemental Figure S4), but to a lower extent than Rac1, and we showed that Cdc42 (and RhoA) are both dispensable for the LLO-mediated entry pathway.

Why does *L. monocytogenes* use multiple invasins and invasion strategies?

Listeria monocytogenes infects multiple nonphagocytic cell types, including enterocytes, hepatocytes, cardiac myocytes, neurons, cytotrophoblasts, endothelial cells, and so on. It is therefore not surprising that this pathogen evolved to express multiple strategies to invade host cells. The major *L. monocytogenes* invasin, InlA, acts by attaching the bacterium to the cell adhesion molecule E-cadherin but not all cell types infected by *L. monocytogenes* express E-cadherin (Gaillard *et al.*, 1991; Mengaud *et al.*, 1996; Ortega *et al.*, 2017). The second invasion protein InlB acts via activating c-Met and was shown to cooperate with InlA to potentiate the bacterial internalization pathway (Dramsi *et al.*, 1995; Shen *et al.*, 2000; Pentecost *et al.*, 2010; Gessain *et al.*, 2015). Although the initial stage of activation of bacterial internalization differs for each invasin (InlA binds to E-cadherin, InlB activates c-Met, LLO forms pores) they all converge toward activation of Rho GTPases and the Arp2/3 complex leading to F-actin– and dynamin-dependent internalization (Ribet and Cossart, 2015). More recently it was shown that the InlB internalization pathway involves a PKC similarly to our finding with LLO (Bhalla *et al.*, 2017). InlA, InlB, and LLO are coexpressed and may cooperate to activate a more robust endocytic signaling in normally nonphagocytic cells. Alternatively, the invasins may promote *L. monocytogenes* invasion in a cell-type–dependent manner.

Overall, this work confirms the novel concept that pathogens use host cell plasma membrane damage as a strategy to induce their endocytic uptake into normally nonphagocytic cells, thereby ensuring the first step of their intracellular life cycle. Unlike previous studies, this work proposes that the plasma membrane resealing pathway is a prerequisite but is not directly responsible for pathogen uptake. We propose that in the example of *L. monocytogenes*, a Ca^{2+}-dependent pathway that is distinct from plasma membrane resealing is activated downstream from cell injury to restore the cortical actin cytoskeleton, which is hijacked for pathogen internalization.

MATERIALS AND METHODS

Reagents and inhibitors

Cells were pretreated for 1 h with the following pharmacological inhibitors (Sigma-Aldrich): kanamycin (30 µg/ml), ampicillin (100 µg/ml), chloramphenicol (5 µg/ml), CK-636 and CK-666 (50–150 µM), GF109203x (0.05–1.0 µM), and Gö6983 (0.5 µM). Cells were pretreated for 10 min with cytochalasin D (1 µM; Sigma-Aldrich). Antibodies include the following: anti–*L. monocytogenes* rabbit polyclonal antibodies (GeneTex); goat anti-rabbit secondary antibodies conjugated to Alexa488 and Alexa568 (Molecular Probes); anti-BSA rabbit antiserum (B1520; Sigma-Aldrich); mouse monoclonal antibodies directed against Rac1, RhoA, and Cdc42 (clones ARC03, ARH04, and ACD03, respectively; Cytoskeleton); rabbit anti-actin (clone A2103; Sigma-Aldrich); and secondary goat anti-mouse immunoglobulin G (IgG) and goat anti-rabbit IgG antibodies conjugated to horseradish peroxidase (Cell Signaling). FluoSpheres carboxylate modified microspheres (1 µm) (Molecular Probes), BSA (Santa Cruz Biotechnology), and 1-ethyl-3-(3-dimethylaminopropyl) carbodiimide hydrochloride (Thermo-Fisher) were used to prepare the beads for LLO coating. Lipofectamine RNAiMax and Lipofectamine 2000 (Life Technologies) were used to transfect siRNA

and plasmid DNA, respectively, using the manufacturer's protocols. Silencer select siRNA for Rac1, RhoA, Cdc42, and NC were used at 60–90 pg per well in a six-well format (Life Technologies).

Listeriolysin O purification

Escherichia coli BL21(DE3) containing pET29b *hly*, which encodes a C-terminal 6His-tagged listeriolysin O missing the signal sequence (N-terminal 25 amino acids), or pET29b *hly* (G80C, S215C), which encodes a C-terminal 6His-tagged listeriolysin O missing the signal sequence (N-terminal 25 amino acids) and contains two amino acid substitutions (G80C, S215C) to produce the prepore locked variant LLOpL, were grown on Luria broth (LB) agar containing 30 μg/ml kanamycin at 37°C overnight. Bacterial cultures were grown overnight at 37°C in LB-supplemented kanamycin (30 μg/ml). The overnight culture was subcultured in 0.5 l LB supplemented with kanamycin and grown to OD_{600} = 0.6 at which point isopropyl β-D-1-thiogalactopyranoside (1 mM final concentration) was added to induce expression of the 6His-tagged listeriolysin O and the culture was agitated at room temperature for 5 h. The culture was pelleted at 6000 × *g* for 10 min. All buffers used for the LLOpL purification lacked beta-mercaptoethanol (BME) and dithiothreitol (DTT). Cell pellets were suspended in lysis buffer (50 mM phosphate, pH 8.0, 1 M NaCl, 5 mM BME, and protease inhibitor) and lysed using a French press. Cell lysate was centrifuged and the supernatant was applied to Ni-NTA Agarose (Qiagen) for 2 h at 4°C. The agarose was washed with (50 mM phosphate, pH 6, 1 M NaCl, 20 mM imidazole, 5 mM BME, 0.1% Tween-20, 10% glycerol) followed by two washes with (50 mM phosphate, pH 6, 1 M NaCl, 20 mM imidazole, 5 mM BME). The protein was eluted with (50 mM phosphate, pH 6, 1 M NaCl, 500 mM imidazole, 5 mM BME) and dialyzed in 50 mM phosphate, pH 6, 0.5 M NaCl, 5 mM DTT.

Bacterial cultures

Wild-type *L. monocytogenes* (strain 10403s) and its isogenic *hly* deletion mutant were gifts from Dan Portnoy (University of California, Berkeley). Bacterial cultures were grown overnight at 37°C under agitation in brain and heart infusion (BHI; BD Biosciences). *Escherichia coli* XL1blue and DH5α were grown at 37°C under agitation in LB supplemented with kanamycin (30 μg/ml), ampicillin (100 μg/ml), or chloramphenicol (5 μg/ml).

Plasmid construction and purification

Escherichia coli XL1Blue harboring the plasmids pmECFP-C1, pmEYFP-C1, pECFP-YFP, pmECFP-PBD, pmEYFP-Rac1, pmEYFP-Rac1-T17N, and pmEYFP-Rac1-H40Y/Q61L were prepared as described previously (Hoppe *et al*., 2002, Hoppe and Swanson, 2004). Sanger sequencing with primers A and B was used to verify insert sequences (Supplemental Table S6). To obtain the constitutively active form of Rac1 (pmEYFP-Rac1-Q61L), pmEYFP-Rac1-H40Y/Q61L was mutated via site-directed mutagenesis using primers C and D. Sanger sequencing with primers A and B was used to verify that the proper mutation was made. *Escherichia coli* DH5α containing pcDNA3-hPKCβII-YFP, pcDNA3-hPKCε-HA1-GFP, and pcDNA3-hPKCδ-HA1-GFP and *E. coli* XL1Blue containing pEGFP-PKCα were gifts from Alexandra Newton (University of California, San Diego) (Antal *et al*., 2014). *Escherichia coli* containing pcDNA3 constructs was grown in LB supplemented with 100 μg/ml ampicillin while *E. coli* containing pEGFP constructs was grown in LB supplemented with 30 μg/ml kanamycin. *Escherichia coli* DH5α containing pcDNA3 MyrPalm-CKAR was grown in LB supplemented with 100 μg/ml ampicillin (Addgene) (Violin *et al*., 2003). Plasmids pEGFPN1 and pEGFP-PKCα were submitted for Sanger sequencing using primers E and G and E, F, and G, respectively (Supplemental Table S6). The GenElute Endotoxin-free Plasmid Midiprep Kit was used to purify endotoxin-free plasmids according to the manufacturer instructions (Sigma-Aldrich).

Mammalian cell culture, silencing, and transfection

The human hepatocyte carcinoma cell line HepG2 (ATCC HB-8065) was grown in MEM with Earle's salts and 2 mM L-glutamine supplemented with 10% heat-inactivated fetal bovine serum (FBS; Lonza), 0.1 mM nonessential amino acids, 1 mM sodium pyruvate, 100 U/ml penicillin, and 100 μg/ml streptomycin (Invitrogen). Cells were grown at 37°C in a 5% CO_2 humidified cell culture incubator. Cells were seeded at 1×10^4 cells/well in a 24-well tissue culture plate, 4×10^5 cells/dish in No. 1.5, 10-mm glass diameter MatTek dish for live cell imaging, or 5×10^5 cells/well in six-well tissue culture plates containing 22 × 22 mm No. 1.5 cover glass (Gold Seal). To silence the expression of the Rho GTPases, cells were transfected in antibiotic-free medium using Lipofectamine RNAi Max (Invitrogen) with silencer select siRNA for Rac1, RhoA, Cdc42, or negative control siRNA. The media was replaced 24 h after seeding and incubated for an additional 24 h. To monitor Rho GTPase activation by FRET microscopy, cells were seeded at 4×10^5 cells in 35 mm No. 1.5, 10-mm-diameter glass MatTek dishes (MatTek P35GC-1.5-10-C). Twenty-four hours after seeding, cells were transfected with 2500 μg total plasmid DNA in antibiotic- and serum-free medium using Lipofectamine 2000 (ThermoFisher Scientific). Serum was added to a final 10% after 1 h, and then the cell culture media was replaced with antibiotic-free medium after an additional 1 h.

Western blot analysis for Rac1, RhoA, and Cdc42 in HepG2 expression

After 48 h of treatment with, or without (control, nontreated), the siRNAs, HepG2 cells were washed once with PBS, pH 7.4, and lysed in 100 μl boiling reduced sample buffer. Cell lysates were boiled for 5 min and equivalent to 1.5×10^5 (nondiluted), 7.5×10^4 (1:2 dilution), 3.75×10^4 (1:4 dilution), and 1.88×10^5 (1:8 dilution) cells were loaded into a 10% SDS–PAGE. All samples were subjected to SDS–PAGE and Western blot analysis using Rac1, RhoA, Cdc42, and actin antibodies, followed by a goat anti-mouse IgG conjugated to HRP or goat anti-rabbit IgG conjugated to HRP. Western blots were developed using the Amersham ECL Select Detection Reagent (GE Healthcare Life Sciences) and imaged using a ChemiDoc XRS+ system and ImageLab software (Bio-Rad). Once the conditions for knockdown were established, at least three independent experiments were performed to confirm efficient silencing, and Western blot analyses were performed in each experiment to verify knockdown efficiencies.

Densitometry analysis. Nontreated and siRNA-treated HepG2 cell lysates were processed for Western blot analysis. Densitometry analysis using ChemiDoc XRS+ system and ImageLab software (Bio-Rad) was performed to assess band intensities (verified for nonsaturation), and all values were normalized relative to NC siRNA-treated sample. The ratio of Rho GTPase to actin was then calculated to compare the Rho GTPases expression levels (Supplemental Table S1).

Bacterial invasion assay

Overnight cultures of *L. monocytogenes* were diluted 1:20 in BHI and grown at 37°C to mid–log phase at an OD_{600} = 0.8. Bacteria were washed 3 times in phosphate-buffered saline (PBS), pH 7.4, diluted into MEM at a multiplicity of infection (MOI) 20 and added to the mammalian cells that were seeded at 5×10^5 cells/well in a

24-well plate and cultured for 48 h. Cell culture plates were centrifuged at 520 × *g* for 3 min at room temperature and incubated for 30 min at 37°C. Infected cells were washed with MEM twice followed by two additional washes in PBS and fixed with 4% paraformaldehyde (PFA) in PBS, pH 7.4, for 15 min at room temperature. Cells were washed three times with 0.1 M glycine in PBS and blocked in 0.1 M glycine in PBS/10% FBS for 1 h. For labeling, extracellular bacteria were labeled with the primary anti–*L. monocytogenes* antibody and secondary anti-rabbit antibody conjugated to Alexafluor-488, and total bacteria were labeled, after cell permeabilization with 0.5% TX-100 (in PBS), with a primary anti–*L. monocytogenes* rabbit polyclonal antibody and a secondary anti-rabbit antibody conjugated to Alexafluor-568. Cells were preserved in Prolong Gold Antifade Mountant medium containing 4′,6 diamidino-2-phenylindole, dihydrochloride (DAPI). To quantify the numbers of bacteria, 40 sets of images (DAPI, Alexa-488, Alexa-568, and phase-contrast) were randomly acquired using a Metamorph programmed, motorized stage and the 20× objective. Metamorph imaging and analysis software were used to determine the number of extracellular (Ne) and total (Nt) bacteria such that the efficiency of bacterial entry was measured as the percentage of intracellular bacteria (Ni) using the equation Ni = (Nt – Ne)*100/Nt.

Polystyrene beads invasion assay

FluoSpheres carboxylate-modified microspheres (1 µm) (blue fluorescent 365/415) were washed with 15 mM NaoAc, pH 5, three times; incubated with 5 mg/ml BSA in 15 mM NaoAc, pH 5; and treated with 0.008 g 1-ethyl-3-(3-dimethylaminopropyl) carbodiimide hydrochloride and 0.1 N NaOH at 4°C overnight to covalently coat the beads with BSA. The following day, 2.5 M glycine was added for a 30-min incubation followed by two washes in 0.33× PBS, pH 7.4 (Gedde *et al.*, 2000). Beads were washed twice with ice-cold buffer A (20 mM HEPES, pH 7.5, 50 mM NaCl, 1 mM $NiCl_2$), suspended in ice-cold buffer B (20 mM HEPES, pH 7.5, 50 mM NaCl) and 5 µg LLO (or none) to adsorb LLO to the surface, and incubated on ice for 10 min. Two washes with buffer B removed excess LLO, and beads were diluted into ice-cold MEM to obtain MOI 5 or 20. Beads were added to mammalian cells in a six- or 24-well plate format followed by centrifugation at 520 × *g* for 3 min at room temperature and incubated for 30 min at 37°C. Cells were washed with MEM twice followed by two washes with PBS and fixed with 4% paraformaldehyde (PFA) in PBS, pH 7.4, for 15 min at room temperature. Cells were washed three times with 0.1 M glycine in PBS, pH 7.4, and blocked in 0.1 M glycine in PBS/5% milk for 1 h. Extracellular beads were labeled using an anti-BSA rabbit antiserum followed by a secondary goat anti-rabbit IgG antibody conjugated to Alexa-488. To quantify the number of intracellular beads, 40 sets of images (DAPI, Alexa-488, and phase-contrast) were randomly acquired using a Metamorph programmed, motorized stage, and the 20× objective. Metamorph imaging and analysis software was used to determine the number of extracellular (Alexa-488, Ne) and total (DAPI, Nt) beads such that the efficiency of bead entry was measured as the percentage of intracellular beads (Ni) using the equation Ni = (Nt – Ne)*100/Nt.

Microscope equipment

A motorized, atmosphere-controlled inverted wide-field fluorescence microscope (Axio Observer D1; Carl Zeiss) equipped with a PZ2000 XYZ Series Automated Nano stage (Applied Scientific Instruments); a TempModule S1, Heating Unit XL S, and Objective heater 22.5/34 S1 (D) (Carl Zeiss); 20X Plan Neofluar, 40X Plan Neofluar, and 100× Plan Apo objective lenses (NA = 0.5, 1.3, 1.4, respectively); Cascade II:512 electron-multiplying charge-coupled device (EMCCD) camera (Photometrics); ORCA-FLASH4.0 V2 Digital complementary metal-oxide-semiconductor camera (Hamamatsu); and a Smart Shutter (Sutter Instrument) on the LED lamp. A Lambda 10-3 optical emission filter changer and DG-4 ultra-high-speed wavelength switching illumination system with a 300-W Xenon arc bulb (Sutter Instrument Company) equipped with excitation filters for CFP and FRET (S430/25x) and for YFP (S500/20x), emission filters for CFP (S470/30) and for YFP and FRET (S535/30), and a JP4 beamsplitter for CFP and YFP (86002v2-spr) from Chroma Technology, were controlled with Metamorph Microscopy Automation and Image Analysis Software (Molecular Devices).

FRET stoichiometry imaging

Fluorescence resonance energy transfer or FRET is a biochemical technique that assesses the physical proximity of fluorophores at distances ≤10 nm. On excitation, a donor fluorophore transfers its energy in a nonradiative manner to a lower energy acceptor fluorophore leading to acceptor fluorescence. FRET stoichiometry utilizes donor emission at donor excitation wavelength (I_D), acceptor emission at acceptor excitation wavelength (I_A), and acceptor emission at donor excitation wavelength (I_F) to quantify FRET. FRET stoichiometry relies on four predetermined coefficients (α, β, γ, and ξ) that are characteristic of the microscope settings and fluorophores used (Hoppe *et al.*, 2002, Hoppe and Swanson, 2004). The coefficients were determined using HepG2 cells expressing mCit alone (α = 0.072), mCFP alone (β = 0.584) and mCit-mCFP tandem (γ = 0.058 and ξ = 0.0156).

Phase-contrast (PC), I_D, I_A, and I_F images were acquired with the Cascade II:512 EMCCD camera (Photometrics) at 200-ms exposure every 20 s over 20 min, in which no photobleaching was observed. Images were corrected for camera dark noise and adjusted with a binary mask, and FRET stoichiometry was applied to determine, pixel by pixel, E_A and E_D using the Metamorph software. The apparent FRET efficiency E_A is proportional to the fraction of mCit in complex with mCFP, while E_D is proportional to the fraction of mCFP in complex with mCit (Hoppe *et al.*, 2002). The average apparent FRET efficiency, $E_{AVE} = (E_A+E_D)/2$, corrects for variations in donor and acceptor expression levels and therefore normalizes FRET signals among different transfected cells (Beemiller *et al.*, 2006).

FRET stoichiometry measurements between mCit-Rac1 and mCFP-PBD

HepG2 cells cotransfected to express mCit-Rac1 and mCFP-PBD, or the mentioned chimeras, were imaged for PC, I_D, I_A, and I_F under 40× magnification. Cells were imaged in microscopy cell culture medium (150 mM NaCl, 1 mM $CaCl_2$, 1 mM $MgCl_2$, 5 mM KCl, 20 mM HEPES, 10 mM D + glucose) or Ca^{2+}-free microscopy cell culture medium. FRET stoichiometry was applied to each image, pixel by pixel, using I_D, I_A, and I_F to create a calculated image corresponding to $E_{AVE} = (E_A + E_D)/2$ or FRET. As controls for Rac1 FRET analysis, we quantified the apparent FRET efficiency in cells that coexpressed mCFP-PBD plus the mCit fluorophore alone (FRET negative control), the native mCit-Rac1 (control for basal Rac1 activity), the dominant negative mCit-Rac1N17 (negative control for Rac1 activation), and the constitutively active mCit-Rac1L61 (positive control for Rac1 activation). Additionally, cells separately expressing mCFP and mCit (FRET negative control), or the FRET pair mCit-mCFP tandem (FRET-positive control for the two fluorophores), were analyzed for FRET efficiency. Cells were placed on the microscope stage at 37°C, and image series

were collected every 20 s for 20 min (Supplemental Figure S1 and Supplemental Movie S1). In cells that coexpressed mCit-Rac1 and mCFP-PBD and exposed to LLO and/or inhibitors, FRET (E_{AVE}) was calculated within two standard regions (305 pixels) that were positioned on each cell, at each time point. For each region, the average FRET value over the first 5 min of imaging (before the addition of medium or LLO) was calculated to determine the baseline FRET within the analyzed region; all data points were then normalized relative to this value. In cells exposed to LLO and control nontreated cells, the regions were positioned where Rac1 FRET variations were observed. If no FRET variation were observed, then the two regions were arbitrarily positioned at the cell periphery. A FRET-positive cell was determined as a cell that displayed at least a twofold increase in normalized FRET efficiency.

FRET measurements of the MyrPalm-CKAR biosensor

The C kinase activity reporter (CKAR) encoded in pcDNA3.1(+) is a chimeric protein containing an N-terminal mCFP fused to the Rad53p FHA2 domain, followed by an optimal substrate sequence for all PKC isoforms and a C-terminal mYFP (mCit). A 10-residue sequence from Lyn Kinase, which signals for myristoylation and palmitoylation, is located at the N-terminal end of the reporter resulting in the plasma membrane associated reporter MyrPalm-CKAR. In a nonphosphorylated state, the reporter exists in a clamped conformation resulting in FRET between mCFP and mCit. On substrate sequence phosphorylation by a PKC, the FHA2 phosphopeptide domain binds the phosphorylated sequence resulting a conformational change moving mCit away from mCFP resulting in a loss of FRET. Importantly, this PKC biosensor has a dynamic range of 20% (Violin *et al.*, 2003; Gallegos and Newton, 2011). FRET stoichiometry was applied to each image, pixel by pixel, using HepG2 cells transfected to express MyrPalm-CKAR. Cells were washed once with microscopy cell culture medium (150 mM NaCl, 1 mM $CaCl_2$, 1 mM $MgCl_2$, 5 mM KCl, 20 mM HEPES, 10 mM D-glucose) and incubated in the same medium for 1 h at 37°C prior to imaging. The I_D, I_A, and I_F images were acquired with the Cascade II:512 EMCCD camera (Photometrics) at 200-ms exposure time every 20 s for 20 min under 100× magnification. FRET stoichiometry was applied to each image, pixel by pixel, using I_D, I_A, and I_F to create a calculated image corresponding to $E_{AVE} = (E_A + E_D)/2$ (or FRET) and E_{AVE} was averaged over the entire cell surface at each time point. The FRET values were normalized relative to E_{AVE} averaged over the first 5 min before the addition of medium or LLO.

Membrane repair assay

HepG2 cells were seeded in a 96-well black-walled and clear bottom cell culture plate at 5×10^4 cells/well in 200 µl and incubated for 24 h. For Ca^{2+}-containing conditions, cells were washed twice with 200 µl M1 (Hank's balanced salt solution [HBSS] supplemented with 0.5 mM $MgCl_2$, 1.2 mM $CaCl_2$, 10 mM HEPES, 25 mM glucose, pH 7.4) at 37°C. For the Ca^{2+}-free condition, cells were washed once with M2 (HBSS supplemented with 0.5 mM $MgCl_2$, 10 mM HEPES, 25 mM glucose, pH 7.4) containing 5 mM EGTA and twice with M2 at 37°C. M1 or M2 (100 µl) was added to the respective wells. Reagents were added to a separate 96-well plate maintained on ice: 100 µl of 120 µM PI in medium containing Ca^{2+} (M1) or not (M2), plus 100 µl of 4×-concentrated LLO (M1 or M2). The amount of 100 µl of medium containing the reagents were then transferred to the plate containing the cells. Additionally, as a positive control of plasma membrane damage, 0.1 and 1% Triton X-100 was added in place of LLO. As a negative control, M1 alone and M1 containing PI was added. HepG2 cells were exposed to 0.25, 0.5, and 1 nM LLO (final concentration) in M1 or M2. The kinetics assay was performed on a Spectra Max i3X Multi Mode Detection Platform (Molecular Devices) with the following parameters: 37°C, fluorescence readings every 5 min for 30 min with an excitation/emission filter of 535/617 and 15/15 nm bandwidth (Pathak-Sharma *et al.*, 2017).

Erythrocyte isolation and hemolysis assays

Human peripheral blood was obtained from healthy adult volunteer via venipuncture (Institutional Review Board protocol H0045). All donors provided a written informed consent. Erythrocytes were separated from plasma, leukocytes, and platelets by centrifugation on Polymorphprep (Axis-Shield) and erythrocytes were washed three times with Alsever's Solution (71.9 mM NaCl, 27 mM $C_6H_5Na_3O_7{\cdot}2H_2O$, 2.6 mM $C_6H_5Na_3O_7{\cdot}H_2O$, 113.8 D-glucose).

Hemolysis assay (end point). Erythrocytes (5×10^7 cells/ml) were suspended in PBS or in PBS containing 4 mM DTT. LLO or LLOpL were serially diluted in PBS or PBS containing 4 mM DTT in 10 µl in a 96-well cell culture plate, and 150 µl of erythrocytes in the respective media was added. Erythrocytes were incubated at 37°C for 30 min and then centrifuged at 343 × *g* for 5 min. Supernatant (100 µl) from each well was transferred to a new 96-well cell culture plate, and OD = 540 nm was measured using the Spectra Max i3X Multi Mode Detection Platform (Molecular Devices).

Hemolysis assay (kinetics). Erythrocytes were suspended in ice-cold PBS containing DMSO vehicle control, 1 mM cytochalasin D, 1 mM GF109203x, or 150 µM CK-666 to a concentration of 5×10^7 cells/ml. LLO (10 nM) in PBS containing DMSO vehicle control, 1 mM cytochalasin D, 1 mM GF109203x, or 150 µM CK-666 was distributed in 10-µl aliquots in a 96-well cell culture plate that was placed on ice. Erythrocytes (150 µl) were added, and the plate was placed in the Spectra Max i3X Multi Mode Detection Platform (Molecular Devices). The OD = 700 nm was measured every min for 30 min at 37°C.

Statistics

In the entire article, "*n*" refers to the number of independent experiments. Statistical analyses were performed as follows.

Invasion assays. A linear mixed effects model was used to take account of the correlation among observations obtained from the same day and Holm's procedure was used to control for multiple comparisons.

Rac1 FRET and MyrPalm-CKAR FRET. The area under the FRET curve (AUC) between time points T_0 (LLO addition), and T_{15} min (end of the movies) in cell culture with Ca^{2+}, or T_0 and T_5 in cell culture without Ca^{2+}, was calculated and analyzed using the Student's *t* test for unequal variances and analysis of variance, respectively (Supplemental Tables S2 and S3 for Rac1 FRET and Supplemental Tables S4 and S5 for MyrPalm CKAR FRET). When comparing the percentage of FRET-positive cells for the Rac1 FRET (Supplemental Tables S2 and S3), linear mixed effects models were used to account for repeated experiments. Holm's procedure was used to adjust the *p* values (Pathak-Sharma *et al.*, 2017) for all the above multiple comparisons. SAS9.4 was used for the analyses (SAS Institute).

Membrane repair. Propidium iodide (PI) intensity values were first background corrected, $\log_{10}$-transformed, and averaged for a given condition for each time point for each experiment. Negative values were set to 0 after transformations. The fixed effects of conditions with DMSO or the inhibitors GF109203x, CK-666, and cytochalasin

D, time (as a continuous variable), and LLO concentration (as a categorical variable) were tested with a linear mixed model to take into account the correlation among observations from the same independent replicates using the average log-transformed intensity values. A pairwise comparison was made between the different LLO concentrations (0, 0.25, 0.5, and 1 nM) and their differences on $\log_{10}$ (intensity), and the same analysis was performed on the different inhibitor conditions (DMSO, 1 μM cytochalasin D, 1 μM GF109203x, and 150 μM CK-666) (Supplemental Table S5). Holm's procedure was used to adjust the *p* values (Pathak-Sharma *et al.*, 2017) for all above multiple comparisons. SAS9.4 was used for the analyses (SAS Institute).

ACKNOWLEDGMENTS

We acknowledge Alexandra Newton (University of California, San Diego) for providing guidance for the study of PKC activation and providing PKC encoding plasmids. We thank Daniel Wozniak for editing. Research reported in this article was supported by the National Institute of Allergy and Infectious Diseases of the National Institutes of Health under award number RO1AI107250 to Stephanie M. Seveau and award number 1-T32-AI-112542, a NRSA training grant administered by the Center for Microbial Interface Biology at The Ohio State University to Sarika Pathak-Sharma. The content is solely the responsibility of the authors and does not necessarily represent the official views of the National Institutes of Health.

REFERENCES

Andrews NW, Almeida PE, Corrotte M (2014). Damage control: cellular mechanisms of plasma membrane repair. Trends Cell Biol 24, 734–742.

Antal CE, Violin JD, Kunkel MT, Skovso S, Newton AC (2014). Intramolecular conformational changes optimize protein kinase C signaling. Chem Biol 21, 459–469.

Beemiller P, Hoppe AD, Swanson JA (2006). A phosphatidylinositol-3-kinase-dependent signal transition regulates ARF1 and ARF6 during Fcgamma receptor-mediated phagocytosis. PLoS Biol 4, e162.

Bergelson JM, Cunningham JA, Droguett G, Kurt-Jones EA, Krithivas A, Hong JS, Horwitz MS, Crowell RL, Finberg RW (1997). Isolation of a common receptor for Coxsackie B viruses and adenoviruses 2 and 5. Science 275, 1320–1323.

Bhalla M, Law D, Dowd GC, Ireton K (2017). Host serine/threonine kinases mTOR and protein kinase C-alpha promote InlB-mediated entry of Listeria monocytogenes. Infect Immun 85, e00087-17.

Brumell JH, Grinstein S (2003). Role of lipid-mediated signal transduction in bacterial internalization. Cell Microbiol 5, 287–297.

Chesarone MA, Goode BL (2009). Actin nucleation and elongation factors: mechanisms and interplay. Curr Opin Cell Biol 21, 28–37.

Cooper ST, McNeil PL (2015). Membrane repair: mechanisms and pathophysiology. Physiol Rev 95, 1205–1240.

Corrotte M, Almeida PE, Tam C, Castro-Gomes T, Fernandes MC, Millis BA, Cortez M, Miller H, Song W, Maugel TK, Andrews NW (2013). Caveolae internalization repairs wounded cells and muscle fibers. Elife 2, e00926.

Cossart P, Helenius A (2014). Endocytosis of viruses and bacteria. Cold Spring Harb Perspect Biol 6, a016972.

Cossart P, Sansonetti PJ (2004). Bacterial invasion: the paradigms of enteroinvasive pathogens. Science 304, 242–248.

Cox D, Chang P, Zhang Q, Reddy PG, Bokoch GM, Greenberg S (1997). Requirements for both Rac1 and Cdc42 in membrane ruffling and phagocytosis in leukocytes. J Exp Med 186, 1487–1494.

Dramsi S, Biswas I, Maguin E, Braun L, Mastroeni P, Cossart P (1995). Entry of Listeria monocytogenes into hepatocytes requires expression of inIB, a surface protein of the internalin multigene family. Mol Microbiol 16, 251–261.

Etienne-Manneville S, Hall A (2002). Rho GTPases in cell biology. Nature 420, 629–635.

Fernandes MC, Cortez M, Flannery AR, Tam C, Mortara RA, Andrews NW (2011). Trypanosoma cruzi subverts the sphingomyelinase-mediated plasma membrane repair pathway for cell invasion. J Exp Med 208, 909–921.

Fernandes MC, Flannery AR, Andrews N, Mortara RA (2013). Extracellular amastigotes of Trypanosoma cruzi are potent inducers of phagocytosis in mammalian cells. Cell Microbiol 15, 977–991.

Gaillard JL, Berche P, Frehel C, Gouin E, Cossart P (1991). Entry of L. monocytogenes into cells is mediated by internalin, a repeat protein reminiscent of surface antigens from gram-positive cocci. Cell 65, 1127–1141.

Galan JE (2009). Common themes in the design and function of bacterial effectors. Cell Host Microbe 5, 571–579.

Gallegos LL, Newton AC (2011). Genetically encoded fluorescent reporters to visualize protein kinase C activation in live cells. Methods Mol Biol 756, 295–310.

Gedde MM, Higgins DE, Tilney LG, Portnoy DA (2000). Role of listeriolysin O in cell-to-cell spread of Listeria monocytogenes. Infect Immun 68, 999–1003.

Gessain G, Tsai YH, Travier L, Bonazzi M, Grayo S, Cossart P, Charlier C, Disson O, Lecuit M (2015). PI3-kinase activation is critical for host barrier permissiveness to Listeria monocytogenes. J Exp Med 212, 165–183.

Gonzalez MR, Bischofberger M, Freche B, Ho S, Parton RG, van der Goot FG (2011). Pore-forming toxins induce multiple cellular responses promoting survival. Cell Microbiol 13, 1026–1043.

Gonzalez-Garcia JR, Machaty Z, Lai FA, Swann K (2013). The dynamics of PKC-induced phosphorylation triggered by Ca2+ oscillations in mouse eggs. J Cell Physiol 228, 110–119.

Groves E, Dart AE, Covarelli V, Caron E (2008). Molecular mechanisms of phagocytic uptake in mammalian cells. Cell Mol Life Sci 65, 1957–1976.

Haghighat AC, Seveau S (2010). Quantification of host-microbe interactions by automated fluorescence microscopy. J Immunol Methods 352, 186–191.

Hall A (2005). Rho GTPases and the control of cell behaviour. Biochem Soc Trans 33(Pt 5), 891–895.

Ham H, Sreelatha A, Orth K (2011). Manipulation of host membranes by bacterial effectors. Nat Rev Microbiol 9, 635–646.

Hamon M, Bierne H, Cossart P (2006). Listeria monocytogenes: a multifaceted model. Nat Rev Microbiol 4, 423–434.

Hetrick B, Han MS, Helgeson LA, Nolen BJ (2013). Small molecules CK-666 and CK-869 inhibit actin-related protein 2/3 complex by blocking an activating conformational change. Chem Biol 20, 701–712.

Hoppe A, Christensen K, Swanson JA (2002). Fluorescence resonance energy transfer-based stoichiometry in living cells. Biophys J 83, 3652–3664.

Hoppe AD, Swanson JA (2004). Cdc42, Rac1, and Rac2 display distinct patterns of activation during phagocytosis. Mol Biol Cell 15, 3509–3519.

Hotze EM, Wilson-Kubalek EM, Rossjohn J, Parker MW, Johnson AE, Tweten RK (2001). Arresting pore formation of a cholesterol-dependent cytolysin by disulfide trapping synchronizes the insertion of the transmembrane beta-sheet from a prepore intermediate. J Biol Chem 276, 8261–8268.

Idone V, Tam C, Goss JW, Toomre D, Pypaert M, Andrews NW (2008). Repair of injured plasma membrane by rapid Ca2+-dependent endocytosis. J Cell Biol 180, 905–914.

Iliev AI, Djannatian JR, Nau R, Mitchell TJ, Wouters FS (2007). Cholesterol-dependent actin remodeling via RhoA and Rac1 activation by the Streptococcus pneumoniae toxin pneumolysin. Proc Natl Acad Sci USA 104, 2897–2902.

Isberg RR (1990). Pathways for the penetration of enteroinvasive Yersinia into mammalian cells. Mol Biol Med 7, 73–82.

Jimenez AJ, Perez F (2017). Plasma membrane repair: the adaptable cell life-insurance. Curr Opin Cell Biol 47, 99–107.

Li E, Stupack D, Bokoch GM, Nemerow GR (1998). Adenovirus endocytosis requires actin cytoskeleton reorganization mediated by Rho family GTPases. J Virol 72, 8806–8812.

Loustalot F, Kremer EJ, Salinas S (2015). The intracellular domain of the coxsackievirus and adenovirus receptor differentially influences adenovirus entry. J Virol 89, 9417–9426.

Luisoni S, Suomalainen M, Boucke K, Tanner LB, Wenk MR, Guan XL, Grzybek M, Coskun U, Greber UF (2015). Co-option of membrane wounding enables virus penetration into cells. Cell Host Microbe 18, 75–85.

Maeda FY, Cortez C, Yoshida N (2012). Cell signaling during Trypanosoma cruzi invasion. Front Immunol 3, 361.

Mellouk N, Enninga J (2016). Cytosolic access of intracellular bacterial pathogens: the Shigella paradigm. Front Cell Infect Microbiol 6, 35.

Mengaud J, Ohayon H, Gounon P, Mege RM, Cossart P (1996). E-cadherin is the receptor for internalin, a surface protein required for entry of L. monocytogenes into epithelial cells. Cell 84, 923–932.

Mercer J, Helenius A (2012). Gulping rather than sipping: macropinocytosis as a way of virus entry. Curr Opin Microbiol 15, 490–499.
Ortega FE, Rengarajan M, Chavez N, Radhakrishnan P, Gloerich M, Bianchini J, Siemers K, Luckett WS, Lauer P, Nelson WJ, Theriot JA (2017). Adhesion to the host cell surface is sufficient to mediate Listeria monocytogenes entry into epithelial cells. Mol Biol Cell 28, 2945–2957.
Osborne SE, Brumell JH (2017). Listeriolysin O: from bazooka to Swiss army knife. Philos Trans R Soc Lond B Biol Sci 372, doi:10.1098/rstb.2016.0222.
Pathak-Sharma S, Zhang X, Lam JGT, Weisleder N, Seveau SM (2017). High-throughput microplate-based assay to monitor plasma membrane wounding and repair. Front Cell Infect Microbiol 7, 305.
Pentecost M, Kumaran J, Ghosh P, Amieva MR (2010). Listeria monocytogenes internalin B activates junctional endocytosis to accelerate intestinal invasion. PLoS Pathog 6, e1000900.
Pizarro-Cerda J, Charbit A, Enninga J, Lafont F, Cossart P (2016). Manipulation of host membranes by the bacterial pathogens Listeria, Francisella, Shigella and Yersinia. Semin Cell Dev Biol 60, 155–167.
Price LS, Langeslag M, ten Klooster JP, Hordijk PL, Jalink K, Collard JG (2003). Calcium signaling regulates translocation and activation of Rac. J Biol Chem 278, 39413–39421.
Ribet D, Cossart P (2015). How bacterial pathogens colonize their hosts and invade deeper tissues. Microbes Infect 17, 173–183.
Rosado CJ, Kondos S, Bull TE, Kuiper MJ, Law RH, Buckle AM, Voskoboinik I, Bird PI, Trapani JA, Whisstock JC, Dunstone MA (2008). The MACPF/CDC family of pore-forming toxins. Cell Microbiol 10, 1765–1774.
Rosselin M, Virlogeux-Payant I, Roy C, Bottreau E, Sizaret PY, Mijouin L, Germon P, Caron E, Velge P, Wiedemann A (2010). Rck of Salmonella enterica, subspecies enterica serovar enteritidis, mediates zipper-like internalization. Cell Res 20, 647–664.
Rougerie P, Miskolci V, Cox D (2013). Generation of membrane structures during phagocytosis and chemotaxis of macrophages: role and regulation of the actin cytoskeleton. Immunol Rev 256, 222–239.
Seveau S (2014). Multifaceted activity of listeriolysin O, the cholesterol-dependent cytolysin of Listeria monocytogenes. Subcell Biochem 80, 161–195.
Seveau S, Bierne H, Giroux S, Prevost MC, Cossart P (2004). Role of lipid rafts in E-cadherin–and HGF-R/Met-mediated entry of Listeria monocytogenes into host cells. J Cell Biol 166, 743–753.
Seveau S, Pizarro-Cerda J, Cossart P (2007). Molecular mechanisms exploited by Listeria monocytogenes during host cell invasion. Microbes Infect 9, 1167–1175.
Shaughnessy LM, Lipp P, Lee KD, Swanson JA (2007). Localization of protein kinase C epsilon to macrophage vacuoles perforated by Listeria monocytogenes cytolysin. Cell Microbiol 9, 1695–1704.
Shen Y, Naujokas M, Park M, Ireton K (2000). InIB-dependent internalization of Listeria is mediated by the Met receptor tyrosine kinase. Cell 103, 501–510.
Simon CM, Vaughan EM, Bement WM, Edelstein-Keshet L (2013). Pattern formation of Rho GTPases in single cell wound healing. Mol Biol Cell 24, 421–432.
Sit ST, Manser E (2011). Rho GTPases and their role in organizing the actin cytoskeleton. J Cell Sci 124(Pt 5), 679–683.
Stow JL, Condon ND (2016). The cell surface environment for pathogen recognition and entry. Clin Transl Immunology 5, e71.
Sukeno A, Nagamune H, Whiley RA, Jafar SI, Aduse-Opoku J, Ohkura K, Maeda T, Hirota K, Miyake Y, Kourai H (2005). Intermedilysin is essential for the invasion of hepatoma HepG2 cells by Streptococcus intermedius. Microbiol Immunol 49, 681–694.
Tam C, Idone V, Devlin C, Fernandes MC, Flannery A, He X, Schuchman E, Tabas I, Andrews NW (2010). Exocytosis of acid sphingomyelinase by wounded cells promotes endocytosis and plasma membrane repair. J Cell Biol 189, 1027–1038.
Vadia S, Arnett E, Haghighat AC, Wilson-Kubalek EM, Tweten RK, Seveau S (2011). The pore-forming toxin listeriolysin O mediates a novel entry pathway of L. monocytogenes into human hepatocytes. PLoS Pathog 7, e1002356.
Vadia S, Seveau S (2014). Fluxes of Ca2+ and K+ are required for the listeriolysin O-dependent internalization pathway of Listeria monocytogenes. Infect Immun 82, 1084–1091.
Van Aelst L, D'Souza-Schorey C (1997). Rho GTPases and signaling networks. Genes Dev 11, 2295–2322.
Vazquez-Boland JA, Kuhn M, Berche P, Chakraborty T, Dominguez-Bernal G, Goebel W, Gonzalez-Zorn B, Wehland J, Kreft J (2001). Listeria pathogenesis and molecular virulence determinants. Clin Microbiol Rev 14, 584–640.
Velge P, Wiedemann A, Rosselin M, Abed N, Boumart Z, Chausse AM, Grepinet O, Namdari F, Roche SM, Rossignol A, Virlogeux-Payant I (2012). Multiplicity of Salmonella entry mechanisms, a new paradigm for Salmonella pathogenesis. Microbiologyopen 1, 243–258.
Violin JD, Zhang J, Tsien RY, Newton AC (2003). A genetically encoded fluorescent reporter reveals oscillatory phosphorylation by protein kinase C. J Cell Biol 161, 899–909.
Wang K, Huang S, Kapoor-Munshi A, Nemerow G (1998). Adenovirus internalization and infection require dynamin. J Virol 72, 3455–3458.
Wiedemann A, Mijouin L, Ayoub MA, Barilleau E, Canepa S, Teixeira-Gomes AP, Le Vern Y Rosselin M, Reiter E, Velge P (2016). Identification of the epidermal growth factor receptor as the receptor for Salmonella Rck-dependent invasion. FASEB J 30, 4180–4191.
Woolsey AM, Burleigh BA (2004). Host cell actin polymerization is required for cellular retention of Trypanosoma cruzi and early association with endosomal/lysosomal compartments. Cell Microbiol 6, 829–838.
Yousuf MA, Lee JS, Zhou X, Ramke M, Lee JY, Chodosh J, Rajaiya J (2016). Protein kinase C signaling in adenoviral infection. Biochemistry, doi:10.1021/acs.biochem.6b00858.